PHYSICAL REVIEW B **88**, 014526 (2013)

Crystallographic, electronic, thermal, and magnetic properties of single-crystal $SrCo_2As_2$

Abhishek Pandey,[1,*] D. G. Quirinale,[1] W. Jayasekara,[1] A. Sapkota,[1] M. G. Kim,[1,2] R. S. Dhaka,[1,†] Y. Lee,[1] T. W. Heitmann,[3]
P. W. Stephens,[4] V. Ogloblichev,[5] A. Kreyssig,[1] R. J. McQueeney,[1] A. I. Goldman,[1] Adam Kaminski,[1] B. N. Harmon,[1]
Y. Furukawa,[1] and D. C. Johnston[1,‡]
[1]*Ames Laboratory and Department of Physics and Astronomy, Iowa State University, Ames, Iowa 50011, USA*
[2]*Materials Sciences Division, Lawrence Berkeley National Laboratory, Berkeley, California 94720, USA*
[3]*The Missouri Research Reactor, University of Missouri, Columbia, Missouri 65211, USA*
[4]*Department of Physics and Astronomy, SUNY at Stony Brook, Stony Brook, New York 11794, USA*
[5]*Institute of Metal Physics, Ural Division of Russian Academy of Sciences, Ekaterinburg 620990, Russia*
(Received 24 June 2013; revised manuscript received 8 July 2013; published 25 July 2013)

In tetragonal $SrCo_2As_2$ single crystals, inelastic neutron scattering measurements demonstrated that strong stripe-type antiferromagnetic (AFM) correlations occur at a temperature $T = 5$ K [Jayasekara *et al.*, arXiv:1306.5174] that are the same as in the isostructural AFe_2As_2 (A = Ca, Sr, Ba) parent compounds of high-T_c superconductors. This surprising discovery suggests that $SrCo_2As_2$ may also be a good parent compound for high-T_c superconductivity. Here structural and thermal expansion, electrical resistivity ρ, angle-resolved photoemission spectroscopy (ARPES), heat capacity C_p, magnetic susceptibility χ, ^{75}As NMR, and neutron diffraction measurements of $SrCo_2As_2$ crystals are reported together with LDA band structure calculations that shed further light on this fascinating material. The c-axis thermal expansion coefficient α_c is *negative* from 7 to 300 K, whereas α_a (the a-axis thermal expansion coefficient) is positive over this T range. The $\rho(T)$ shows metallic character. The ARPES measurements and band theory confirm the metallic character and in addition show the presence of a flat band near the Fermi energy E_F. The band calculations exhibit an extremely sharp peak in the density of states $\mathcal{D}(E \approx E_F)$ arising from a flat $d_{x^2-y^2}$ band, where the x and y axes are along the a and b axes of the Co square lattice, respectively. A comparison of the Sommerfeld coefficient of the electronic specific heat with $\chi(T \to 0)$ suggests the presence of strong ferromagnetic itinerant spin correlations, which on the basis of the Stoner criterion predicts that $SrCo_2As_2$ should be an itinerant ferromagnet, in conflict with the magnetization data. The $\chi(T)$ does have a large magnitude, but also exhibits a broad maximum at ≈ 115 K suggestive of dynamic short-range AFM spin correlations, in agreement with the neutron scattering data. The measurements show no evidence for any type of phase transition between 1.3 and 300 K and we suggest that metallic $SrCo_2As_2$ has a gapless quantum spin-liquid ground state.

DOI: 10.1103/PhysRevB.88.014526 PACS number(s): 74.70.Xa, 75.40.Cx, 74.25.Jb, 75.25.−j

I. INTRODUCTION

After the discovery of high-temperature superconductivity (SC) below $T_c = 26$ K in tetragonal $LaFeAsO_{1-x}F_x$ (1111-type) in 2008,[1] a worldwide effort began to understand the mechanism for the SC and to discover other Fe-based superconductors. This effort quickly led to the enhancement of T_c to its current record among bulk Fe-based superconductors of $T_c = 56.3$ K for the 1111-type compound $Gd_{0.8}Th_{0.2}FeAsO$.[2] Additional families of Fe-based high-T_c superconductors were soon discovered including the 122-type arsenides where the parent compounds have composition AFe_2As_2 (A = Ca, Sr, Ba, Eu) with the tetragonal $ThCr_2Si_2$-type structure (space group $I4/mmm$).[3–5] All families of Fe-based high-T_c superconductors contain stacked square lattices of Fe atoms that are identical to the stacked square lattices of Cu atoms in the layered high-T_c cuprates.[3,6–8]

The 122-type family of iron arsenide-based superconductors is the most studied because large, high-quality single crystals can be grown,[9] and the parent compounds offer enormous flexibility for chemical substitutions on the A, Fe, and As sites. Crystals with masses ∼1 g can be grown, which allows a broad range of measurements including inelastic neutron scattering measurements to be performed to characterize and understand the properties. It has been demonstrated that the parent compounds at ambient pressure exhibit a lattice distortion to an orthorhombic structure at a system-dependent $T_S \lesssim 200$ K together with long-range antiferromagnetic (AFM) ordering at the same or somewhat lower Néel temperature T_N.[3,10] The ordering propagation vector is the same as the nesting wave vector between the hole and electron pockets of the semimetallic band structure. This and the low ordered moments[3,10] $\mu \lesssim 1\,\mu_B$/Fe indicate an itinerant origin of the AFM[11,12] rather than arising from interactions between local Fe magnetic moments.

The AFM structure within the ab plane of the Fe square lattice is a so-called "stripe" structure in which ferromagnetically aligned stripes of Fe magnetic moments along the orthorhombic b axis are AFM aligned along the a axis.[3,10] These orthorhombic axes have the same directions as the respective Fe square lattice a and b axes, which are in turn rotated by 45° with respect to the a and b axes of the body-centered tetragonal $ThCr_2Si_2$-type crystal structure. Furthermore, in order for high-T_c SC to occur, this long-range AFM ordering must be largely suppressed by chemical substitutions or pressure, but strong dynamic short-range AFM correlations must still be preserved. These AFM fluctuations/correlations are widely considered to be the glue for the SC Cooper pairs.[3,11,13,14] A similar phenomenology and temperature-doping phase diagram are found for the high-T_c cuprates.[6–8,15]

Among the substituted 122-type materials,[3] the best studied are $Ba_{1-x}K_xFe_2As_2$ with $T_c \leqslant 38$ K,[16] $Ba(Fe_{1-x}Co_x)_2As_2$

with $T_c \leqslant 25$ K,[17–19] and $BaFe_2(As_{1-x}P_x)_2$ with $T_c \leqslant 30$ K.[20] The detailed temperature-composition phase diagram for $Ba(Fe_{1-x}Co_x)_2As_2$ with $0 \leqslant x \leqslant 0.12$ shows, as $T \to 0$, an AFM region at $0 \leqslant x \lesssim 0.03$, a region of coexisting AFM and SC for $0.03 \lesssim x \lesssim 0.06$ and a region of only SC order (the remaining part of the superconducting dome) for $0.06 \lesssim x \lesssim 0.12$, where $T_c \to 0$ at $x \approx 0.12$.[19] Inelastic neutron scattering measurements demonstrated that the AFM correlations/fluctuations that are present in the paramagnetic (PM) state of $BaFe_2As_2$ above $T_N = 136$ K (Ref. 21) are absent in the nonsuperconducting PM composition $x = 0.14$ at 10 K,[22] consistent with the hypothesis that AFM spin fluctuations are required as the SC pairing glue in these materials.[3,10]

As might be expected from the latter result, neither magnetic susceptibility[18] $\chi(T)$ nor neutron diffraction[23] measurements on $SrCo_2As_2$ showed any evidence for long-range magnetic ordering above 1.8 and 4 K, respectively. This is the same result as found for isostructural $BaCo_2As_2$ (Ref. 24) but is in contrast to the magnetic behavior of $CaCo_2As_2$, which shows A-type AFM ordering below a sample-dependent T_N of 53 to 76 K.[25–27] The $ThCr_2Si_2$-type crystal structure of $SrCo_2As_2$ (Ref. 28) is shown in Fig. 1(a).

The As–As interlayer distance $d_{\rm As-As}$ [see Fig. 1(a)] is correlated with the magnetic ground state,[29] where a "layer" is defined as an As–M–As layer and M is the transition metal, as shown in Fig. 1(b). $CaCo_2As_2$ with an AFM ground state has a collapsed tetragonal (cT) structure reflecting approach to interlayer As–As dimerization, where the As–As single-covalent-bond distance[30] is indicated in Fig. 1(b), whereas $BaCo_2As_2$ with a PM ground state has an uncollapsed tetragonal (T) structure without such dimerization. $SrCo_2As_2$ also has a PM ground state and is in an intermediate regime,[29] as seen in Fig. 1(b). This correlation between the magnetic behavior and the crystal structure contrasts with that of the 122-type AFe_2As_2 compounds where the cT structure of $CaFe_2As_2$ has a nonmagnetic ground state and the T structures of the Ca, Sr, and Ba compounds all have AFM ground states.[3,29,31–33] Interlayer As–As dimerization in the cT phase results in a valence of As^{-2}, i.e., $[As–As]^{-4}$, instead of the usual As^{-3} valence in the 122-type (Ca, Sr, Ba)M_2As_2 compounds, corresponding to a formal M oxidation state of M^{+1} instead of the usual M^{+2}. From Fig. 1(b), $SrCo_2As_2$ may be in a regime with intermediate Co oxidation state between Co^{+1} in $CaCo_2As_2$ and Co^{+2} in $BaCo_2As_2$. This intermediate valence state, in turn, might be expected to result in strong dynamic Co spin fluctuations in $SrCo_2As_2$.

In view of the disappearance of dynamic AFM correlations in the PM state of the $Ba(Fe_{1-x}Co_x)_2As_2$ system as x increases from $x = 0$ to 0.14,[21,22] it is amazing that strong AFM stripe-type correlations are present in the $x = 1$ end-member $SrCo_2As_2$ of the similar series $Sr(Fe_{1-x}Co_x)_2As_2$ (Refs. 34–36) as established from inelastic neutron scattering measurements on single crystals.[23] The above-noted intermediate valence of the Co in $SrCo_2As_2$ may be responsible for the lack of long-range AFM order, at least in part. The presence of these AFM correlations in $SrCo_2As_2$ raises key questions about how they come about in this compound, why this compound is not superconducting, and whether it could be made superconducting by some type of chemical substitution or by application of pressure.

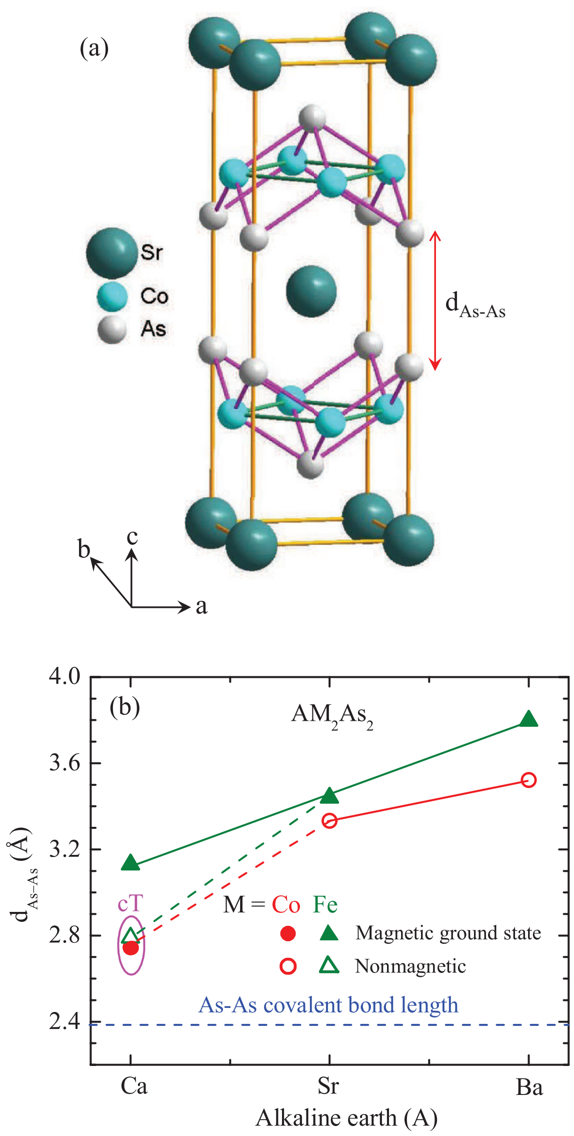

FIG. 1. (Color online) (a) $ThCr_2Si_2$-type body-centered tetragonal crystal structure of $SrCo_2As_2$ with space group $I4/mmm$. The interlayer As–As distance $d_{\rm As-As}$ is indicated. (b) $d_{\rm As-As}$ versus A atom in ACo_2As_2 and AFe_2As_2 (A = Ca, Sr, Ba).[29] The lines are guides to the eye. The horizontal dashed line indicates the As–As single-covalent-bond distance of 2.38 Å.[30]

Here we report the investigation of undoped $SrCo_2As_2$ single crystals using x-ray and neutron diffractions, in-plane (ab-plane) electrical resistivity ρ, angle-resolved photoemission spectroscopy (ARPES), heat capacity C_p, magnetization M, χ, and ^{75}As nuclear magnetic resonance (NMR) measurements, complemented by LDA band structure calculations. Experimental and theoretical details are given in Sec. II. The x-ray diffraction investigations of crushed crystals in Sec. III yield a structure in agreement with previous work. The $\rho(T)$ measurements in Sec. IV demonstrate metallic character, consistent with the ARPES measurements in Sec. V, which also indicate that there is no obvious significant Fermi surface nesting. The band theory calculations in Sec. VI reveal a sharp and high peak in the density of states near the Fermi energy $\mathcal{D}(E \approx E_F)$. The C_p measurements in Sec. VII further confirm the metallic character and confirm the presence of a large $\mathcal{D}(E \approx E_F)$. The M and χ measurements in Sec. VIII show clear evidence for dynamic short-range AFM spin correlations in a quasi-low-dimensional spin lattice, consistent with the inelastic neutron scattering results.[23] The NMR measurements are presented in Sec. IX, which indicate the presence of stripe-type and/or FM correlations. The x-ray diffraction, ρ, C_p, χ, and NMR measurements reveal no obvious phase transitions between 1.3 and 300 K, in agreement with the previous[23] and present neutron diffraction measurements in Sec. X. In Sec. XI, we discuss the ground state of metallic $SrCo_2As_2$ and suggest that this compound has a gapless quantum spin-liquid ground state. A summary and our conclusions are given in Sec. XII.

II. EXPERIMENTAL AND THEORETICAL DETAILS

Single crystals of $SrCo_2As_2$ were grown from solution using Sn flux. In the Fe-based high-T_c superconductivity field, Sn flux was first used by Ni *et al.* to grow crystals of $BaFe_2As_2$ and $Ba_{0.55}K_{0.45}Fe_2As_2$.[37] High-purity elements Sr (99.95%) from Sigma-Aldrich, and Co (99.998%), As (99.99999%), and Sn (99.999%) from Alfa Aesar, were taken in 1:2:2:45 ratio and placed in an alumina crucible that was sealed in an evacuated silica tube. After prereacting the elements at 610 °C for 5 h, the assembly was heated to 1150 °C, left there for 8 h and then slowly cooled to 700 °C in 160 h. At this temperature, the flux was decanted using a centrifuge. The typical size of the crystals obtained was $2 \times 2 \times 0.3$ mm^3. However, by increasing the size of the crucible to a 10 mL capacity, large crystals of $SrCo_2As_2$ with masses up to ≈ 1 g with dimensions up to $15 \times 10 \times 1$ mm^3 can be grown out of Sn flux.[23]

The chemical compositions of the crystals were determined by energy-dispersive x-ray analysis (EDX) using a JEOL-JSM-5910LV scanning electron microscope and found to be in agreement with the expected stoichiometric composition $SrCo_2As_2$. These EDX measurements showed no visible peaks at the expected positions of the Sn x-ray emission lines, and the amount of Sn incorporated into the crystals from the Sn flux was given by the software as 0.22(16) at%, which is consistent with zero to within 1.3σ. However, we cannot rule out the possibility that a very small amount of Sn was incorporated into the crystals, which might have had some influence on the results of our physical property measurements. For comparison, $BaFe_2As_2$ crystals grown in Sn flux contain ∼1 at% Sn as determined using wavelength-dispersive x-ray analysis,[37] which results in large changes in the physical properties such as in a reduction of the tetragonal to orthorhombic structural transition temperature from 136 K in pure crystals grown out of FeAs self-flux as discovered by Wang *et al.*[38] to the value of 85 K in the crystals grown out of Sn flux by Ni *et al.*[37]

Structural characterization was performed using room-temperature powder x-ray diffraction (XRD) data obtained on crushed crystals using a Rigaku Geigerflex powder diffractometer and Cu-K_α radiation. Rietveld refinement of the XRD data was carried out using the FULLPROF package.[39] The $M(H)$, χ, C_p, and four-probe ρ measurements were performed using instruments from Quantum Design, Inc. In the $M(H)$, χ, and C_p measurements, the contribution of the sample holder was measured separately and corrected for in each case.

A high-resolution x-ray powder diffraction pattern was collected at ambient temperature at the beamline X16C at the National Synchrotron Light Source. The sample was ground with an agate mortar and pestle in a glovebox having a water vapor concentration of a few parts per million, loaded into a glass Lindemann capillary of 0.3-mm nominal diameter, and flame-sealed without exposure to the atmosphere. The x-ray wavelength, 0.6995 Å, was chosen using a Si(111) double monochromator. The powder diffraction pattern was collected in the 5–45° 2θ range with a constant step size of 0.005°, and a linearly varying counting time of 1–3 s/point. The incident beam intensity was monitored with an ion chamber and the diffracted radiation was measured with a NaI(Tl) scintillation detector. The axial and in-plane resolution of the diffractometer were set by slits and a Ge(111) analyzer crystal, respectively. Rietveld refinement of the x-ray diffraction pattern was done using the GSAS[40] package.

High-resolution single-crystal x-ray diffraction measurements were performed on a four-circle diffractometer using Cu-$K_{\alpha 1}$ radiation from a rotating anode x-ray source, selected by a Ge(111) monochromator. For measurements of the temperature dependence of the lattice parameters, a platelike single crystal, with the tetragonal c axis perpendicular to the plate, was attached to a flat copper sample holder on the cold finger of a He closed-cycle displex refrigerator. The sample was oriented such that the $(h\ 0\ \ell)$ plane or the $(h\ h\ \ell)$ plane of the reciprocal lattice was coincident with the scattering plane of the diffractometer.

Single-crystal neutron diffraction measurements were done on the TRIAX triple-axis spectrometer at the University of Missouri Research Reactor employing an incident neutron energy of 14.7 meV. A platelike crystal of mass 302.4 mg was mounted on the cold finger of a closed-cycle displex refrigerator with the $(h\ 0\ \ell)$ plane of the reciprocal lattice coincident with the scattering plane of the diffractometer, allowing us to search for magnetic scattering at the reciprocal lattice positions for the A-type AFM structure [$(h\ 0\ \ell)$ with $h + \ell = 2n + 1$], as found previously for $CaCo_2As_2$,[27] and the G-type AFM structure [$(h\ 0\ \ell)$ with h and ℓ odd], as found for the related compound $BaMn_2As_2$.[41]

High-resolution ARPES experiments were carried out using a Scienta R4000 electron analyzer and 140-eV photon energy at beamline 7.0.1 of the Advanced Light Source (ALS), Berkeley, California. The crystals were cleaved *in situ* along the ab plane and measured at a pressure of $\approx 4 \times 10^{-11}$ mbar. The energy and momentum resolution were set to ∼ 20 meV and ∼ 0.3°, respectively. The Fermi energy (E_F) of the sample was referenced to that of a gold sample deposited *in situ* on the sample holder. In our notation, the Brillouin zone (BZ) of $SrCo_2As_2$ is that of the body-centered-tetragonal ($I4/mmm$) direct lattice and not that of the Co square lattice, and the (k_x, k_y, k_z) axes of the Brillouin zone are, as conventionally defined in the literature, in the directions of the direct lattice translation vectors $(\mathbf{a}, \mathbf{b}, \mathbf{c})$, respectively.[3]

Nuclear magnetic resonance (NMR) measurements were carried out on ^{75}As ($I = 3/2$, $\gamma_N/2\pi = 7.2919$ MHz/T) using a homemade phase-coherent spin-echo pulse spectrometer.

TABLE I. Crystal data for ACo_2As_2 (A = Ca, Sr, Ba) compounds that crystallize in the $ThCr_2Si_2$ structure with $I4/mmm$ space group symmetry and $Z = 2$ formula units/unit cell. The A atoms are at the $2a$ (0 0 0) sites, the Co atoms at the $4d$ ($0\ \frac{1}{2}\ \frac{1}{4}$) sites, and the As atoms at the $4e$ ($0\ 0\ z_{\rm As}$) sites. For the laboratory-based measurements, the goodness of fit parameters are $\chi^2 = 1.19$, $R_{\rm p} = 7.08\%$, and $R_{\rm wp} = 9.34\%$, whereas for the synchrotron-based measurements, they are $\chi^2 = 1.08$, $R_{\rm p} = 12.47\%$, and $R_{\rm wp} = 16.67\%$. The designations "T" and "cT" refer to the uncollapsed tetragonal and collapsed tetragonal structures, respectively. $SrCo_2As_2$ has c/a and $d_{\rm As-As}$ values intermediate between those of T-type $BaCo_2As_2$ and cT-type $CaCo_2As_2$.

Compound	a (Å)	c (Å)	c/a	$z_{\rm As}$	$d_{\rm As-As}$ (Å)	Structure	Reference
$CaCo_2As_2$	3.9831(2)	10.2732(6)	2.5792(3)	0.3664(2)	2.745(4)	cT	27 and 29
	3.989(3)	10.33(1)	2.590(9)	0.372	2.64		28
$SrCo_2As_2$	3.9471(4)	11.801(1)	2.9898(6)	0.3588(1)	3.333(3)		This work[a]
	3.9466(2)	11.773(1)	2.9831(4)	0.3587(3)	3.327(7)		This work[b]
	3.935(7)	11.83(2)	3.006(10)	0.362	3.27		28
$BaCo_2As_2$	3.958(5)	12.67(2)	3.201(9)	0.361	3.52	T	28

[a] Laboratory-based x-ray powder diffraction measurements.

[b] Synchrotron-based x-ray powder diffraction measurements.

^{75}As-NMR spectra were obtained by sweeping the magnetic field H at a fixed frequency $f = 51.1$ MHz. The magnetic field was applied parallel to either the crystal c axis or the ab plane. The origin of the NMR shift $K = 0$ of the ^{75}As nucleus was determined by ^{75}As NMR measurements of GaAs. The ^{75}As nuclear spin-lattice relaxation rate ($1/T_1$) was measured with a saturation recovery method.

For electronic structure calculations, we used the full-potential linear augmented plane wave (FP-LAPW)[42] method with the local density approximation (LDA).[43] To obtain self-consistent charge and wave functions, we employed $R_{\rm MT} \times k_{\rm max} = 9.0$ with muffin-tin radii $R_{\rm MT} = 2.3$, 2.1, and 2.1 a.u. for Sr, Co, and As, respectively. 828 **k** points were selected in the irreducible Brillouin zone and calculations were iterated to reach the total energy convergence criterion, which was 0.01 mRy/cell, where a "cell" is a primitive cell containing one formula unit of five atoms. Our experimental lattice parameters in Table I for the $I4/mmm$ structure of $SrCo_2As_2$ ($a = 3.9471$ Å, $c = 11.801$ Å) were used in the calculations. To obtain the theoretical c-axis position $z_{\rm As}$ of the As atom, its position was relaxed until the force on the As atom was smaller than 1 mRy/a.u., which gave $z_{\rm As} = 0.35146$. This value is somewhat smaller than our experimental value $z_{\rm As} = 0.3588(1)$ in Table I.

III. CRYSTALLOGRAPHY AND THERMAL EXPANSION

A. Powder x-ray diffraction: crystal structure

The laboratory-based powder XRD data for $SrCo_2As_2$ are shown in Fig. 2(a), along with the two-phase Rietveld refinement fit including a fit to the adventitious Sn from the flux on the surface of the crystals prior to crushing them, the difference profile and Bragg positions for the main phase as well as for Sn. The parameters fitted during the refinement were the lattice parameters, As c-axis position parameter $z_{\rm As}$, isotropic thermal parameters, scale factor, zero shift, three resolution parameters, profile shape parameter, and asymmetry parameters. The Sn impurity phase fraction was found to be 4.9 wt%. The site occupancies of Sr, Co, and As were kept fixed at 100% during the final refinement cycle because allowing the occupancies to vary from this value did not improve the fit significantly. The lattice parameters and $z_{\rm As}$ are listed in Table I along with the corresponding literature data for $CaCo_2As_2$,

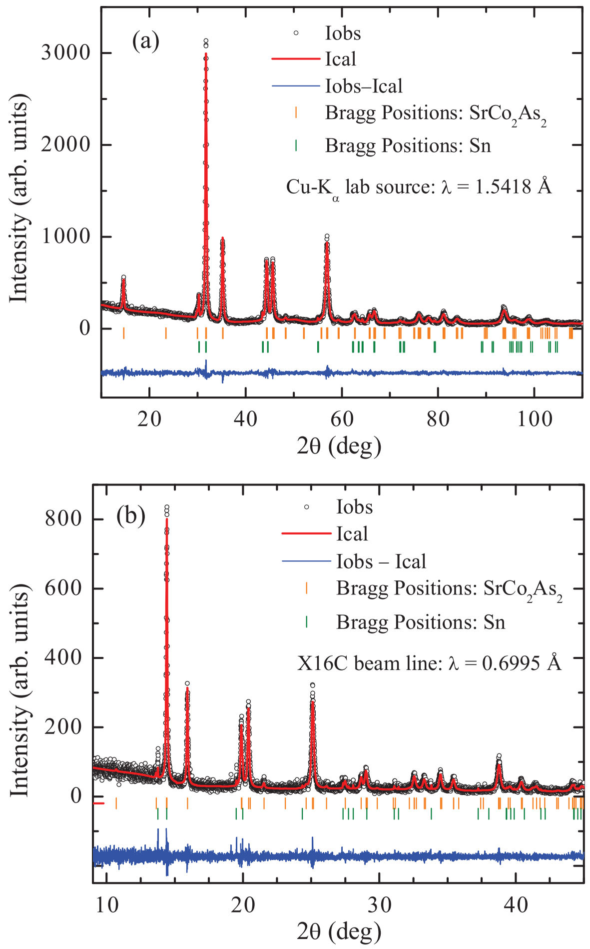

FIG. 2. (Color online) Room-temperature powder XRD data for $SrCo_2As_2$ along with the Rietveld refinement fit, Bragg peak positions, and difference profile from (a) a laboratory-based diffractometer with x-ray wavelength $\lambda = 1.5418$ Å and (b) a synchrotron-based diffractometer with x-ray wavelength $\lambda = 0.6995$ Å. A two-phase Rietveld refinement was performed to account for the peaks from a minor amount of Sn flux on the surfaces of each of the two crushed-crystal samples.

$SrCo_2As_2$, and $BaCo_2As_2$.[27–29] Our data for $SrCo_2As_2$ are in reasonable agreement with those of Ref. 28.

The synchrotron x-ray diffraction pattern for $SrCo_2As_2$, the Rietveld profile refinement fit and residuals are displayed in Fig. 2(b). Here again, an impurity phase of adventitious Sn flux, comprising in this sample approximately 1% of the sample by weight, was included in the refinement of the powder diffraction pattern. A small section of low-angle data was removed from the refinement due to poor statistics. Several very low-intensity peaks could not be identified conclusively with other impurity phases. Table I gives a summary of the results of the refinement of the powder XRD data for the $SrCo_2As_2$ phase. These data are in good agreement with those found above from the laboratory-based x-ray diffraction measurements.

B. Single-crystal x-ray diffraction: thermal expansion and search for a temperature-induced orthorhombic distortion

The T dependencies of the a and c lattice parameters were extracted from the positions of the (2 0 8) and (0 0 8) Bragg peaks measured by single-crystal x-ray diffraction as described in Sec. II. Figure 3(a) shows a striking *decrease* in the c lattice parameter by approximately 0.3% as T *increases* from our base temperature of 7.4 to 300 K, corresponding to a negative thermal expansion coefficient along the c axis over the full T range of the measurement. In contrast, the a lattice parameter *increases* by $\approx 0.35\%$ with increasing T over the same T interval, which corresponds to the usual positive thermal expansion coefficient. The volume thermal expansion in Fig. 3(b) initially decreases on heating above 8 K and then increases from ≈ 80 K to room temperature.

Negative thermal expansion coefficients in the paramagnetic states of materials are unusual. Indeed, the anisotropic thermal expansion coefficients above the coupled structural and magnetic transitions in crystals of the AFe_2As_2 high-T_c parent compounds[44] and in $Ba(Fe_{1-x}Co_x)_2As_2$ crystals with $x = 0.038$ and 0.074 (Ref. 45) are all positive. On the other hand, $Ca_{1-x}La_xFe_2As_2$ crystals with $x = 0.15$, 0.20, and 0.25 all show temperature regions where the a- and/or c-axis and volume expansion coefficients are negative.[46] These latter behaviors are suggested by the authors to originate from proximity to a structural phase transition.

Our thermal expansion data in Fig. 3 reveal no obvious evidence for a temperature-induced lattice distortion in $SrCo_2As_2$. We therefore specifically searched for an orthorhombic lattice distortion, using high-resolution single-crystal x-ray diffraction, that might be associated with the observed negative c-axis and volume thermal expansion coefficients. However, no splitting or changes of peak shape were observed in the temperature range 10–300 K for the (2 0 8) or (1 1 8) reflections measured in the $(h\ 0\ \ell)$ and $(h\ h\ \ell)$ scattering planes, respectively, demonstrating that no tetragonal to orthorhombic lattice distortion occurs over this T range to within an estimated upper limit for a potential distortion of $(a-b)/(a+b) \leqslant 2.5 \times 10^{-4}$.

IV. ELECTRICAL RESISTIVITY

Figure 4 shows the ab-plane $\rho(T)$ of $SrCo_2As_2$. The data exhibit metallic behavior with a high residual resistivity ratio RRR $\equiv \rho(300\ \text{K})/\rho(3\ \text{K}) = 15.3$, indicating good crystal quality. At low temperatures ($3.5\ \text{K} \leqslant T \leqslant 38$ K), we find that $\rho(T)$ follows $\rho = \rho_0 + AT^2$ (inset of Fig. 4) as expected for a Fermi liquid.[47] A fit by this equation gives $\rho_0 = 12.0\ \mu\Omega$ cm and $A = 8.21(4) \times 10^{-3}\ \mu\Omega\ \text{cm/K}^2$.

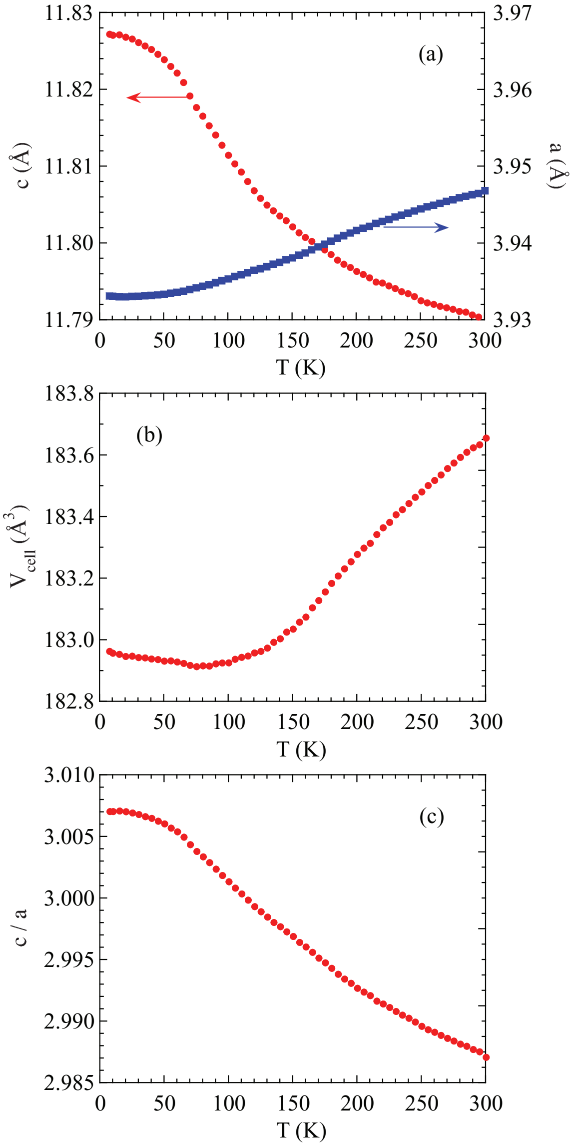

FIG. 3. (Color online) Temperature dependence of (a) the a and c lattice parameters (right- and left-hand ordinates, respectively), (b) unit cell volume $V_{\text{cell}} = a^2c$ and (c) c/a ratio of $SrCo_2As_2$ from single-crystal x-ray diffraction measurements.

The data over the entire T range could not be fitted well solely by the sum of a T-independent term ρ_0 and the Bloch-Grüneisen prediction for carrier scattering by longitudinal lattice vibrations in the absence of umklapp scattering given by[48,49]

$$\rho_{\text{BG}}(T) = 4\mathcal{R}\left(\frac{T}{\Theta_{\text{R}}}\right)^5 \int_0^{\Theta_{\text{R}}/T} \frac{x^5}{(e^x-1)(1-e^{-x})}\,dx, \qquad (1a)$$

where Θ_{R} is the Debye temperature obtained from fitting resistivity measurements and $\mathcal{R}$ is a material-dependent scale

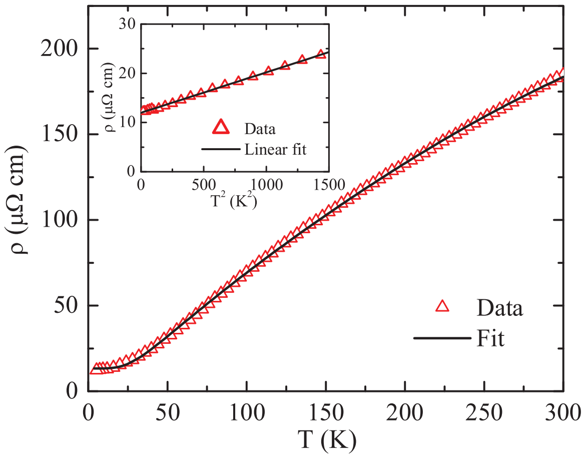

FIG. 4. (Color online) Electrical resistivity ρ measured along the ab plane versus temperature T for $SrCo_2As_2$. The solid curve is a fit by Eqs. (1). Inset: ρ versus T^2, along with a linear fit to the data between 3.5 and 38 K (straight line).

factor that is independent of T. Equation (1a) yields

$$\rho(T = \Theta_R) \approx 0.946\,464\,\mathcal{R}. \tag{1b}$$

At high temperatures $T \gtrsim \Theta_R$, the BG model yields a $\rho_{BG}(T)$ that is proportional to T, whereas the experimental data in Fig. 4 show negative curvature at high T. Therefore we also used a Mott interband sd scattering term $-DT^3$ (Refs. 50,51) to fit the data according to

$$\rho(T) = \rho_0 + \rho_{BG}(T) - DT^3. \tag{1c}$$

This fit function is not accurate at low T because the data below 38 K follow a T^2 dependence as shown in the inset of Fig. 4 and discussed above, whereas $\rho_{BG}(T)$ has a T^5 dependence at low T. Furthermore, we used the high-accuracy analytic dimensionless Padé approximant $\rho_n(T/\Theta_R)$ in Ref. 48 in place of Eq. (1a) to facilitate the least-squares fit to the data, where

$$\rho_{BG}(T) = \rho(\Theta_R)\rho_n(T/\Theta_R). \tag{1d}$$

A good fit of the experimental $\rho(T)$ data in Fig. 4 by Eq. (1) was obtained (black curve in Fig. 4), where the fitted parameters are $\rho_0 = 13.3(1)\ \mu\Omega$ cm, $\rho(\Theta_R) = 104(1)\ \mu\Omega\,$cm, $\Theta_R = 167(1)$ K, and $D = 9.1(1) \times 10^{-7}\ \mu\Omega$ cm K^{-3}. From the value of $\rho(\Theta_R)$ and Eq. (1b), we obtain $\mathcal{R} = 110\ \mu\Omega\,$cm. A significant contribution from the Mott sd interband scattering is expected in materials where narrow d bands appear at the Fermi level, for example in elemental Pd metal.[50] Since the ARPES data and the band structure calculations presented below show that an extremely narrow d band is present at E_F in $SrCo_2As_2$, a substantial contribution from Mott sd interband scattering is not surprising.

V. ARPES

We studied the electronic properties of a $SrCo_2As_2$ single crystal using high-resolution ARPES, which can directly probe the low-energy electronic excitations as a function of binding energy and momentum. Figure 5(a) shows the photoemission intensity map, which is obtained by integrating over an energy window of ±10 meV with respect to the Fermi energy E_F, measured with a photon energy of 140 eV and sample temperature of 90 K. We clearly see four patches of intensity arranged around the center (Γ point) of the Brillouin zone (BZ), which are located at $\pm\pi/a$ along the k_x and k_y directions. More interesting is the observation of a large $\mathbf{k}$-independent intensity near E_F along the $[\pm 1, \pm 1]$ directions passing through the corners (X points) of the BZ. This indicates the presence of a flat band near E_F that extends over a large fraction of the second BZ. Our LDA band structure calculations in Fig. 8(c) below confirm the presence of a flat $d_{x^2-y^2}$ band situated at or very close to E_F that passes through the X points in the $[\pm 1,\pm 1]$ directions, where here the x and y axes are along the a and b axes of the Co square lattice, respectively. A wide flat band just above E_F with an associated very sharp peak in the density of states was also present in previous LDA band calculations for KCo_2As_2.[52]

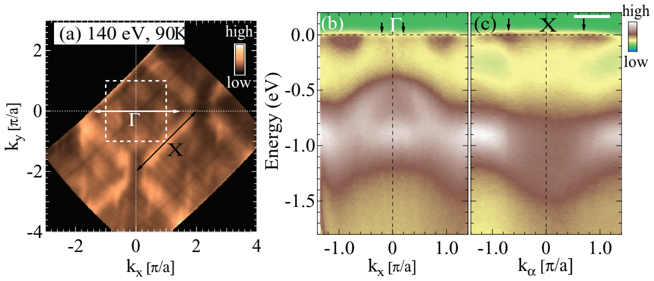

FIG. 5. (Color online) (a) The Fermi surfaces of $SrCo_2As_2$ measured with 140 eV photon energy and at 90 K sample temperature. The photoemission intensity maps are obtained by integrating over an energy window of ±10 meV with respect to the Fermi level. The outline of the first Brillouin zone (BZ) is shown by the white dashed square. (b) Band dispersion data plotted through the center [Γ point, horizontal white line in (a)] of the BZ from $\mathbf{k} = (\sim -\pi/a, 0)$ to $(\sim\pi/a, 0)$ and (c) through the corner [X point $(\pi/a, -\pi/a)$, black line in (a)] of the BZ described by $\mathbf{k} = (\frac{\pi}{a}, -\frac{\pi}{a}) + \mathbf{k}_\alpha$, where $\mathbf{k}_\alpha = (k_\alpha, k_\alpha)$ and k_α ranges from zero to $\approx \pm 1.2\pi/a$. The black vertical arrows at the tops of (b) and (c) denote the Fermi wave vector positions for the electron Fermi surface pockets centered at Γ and X, respectively.

Energy distribution curves (EDCs) for fixed momenta moving along the white line at the top of Fig. 5(c) are shown in Fig. 6(a), and an enlargement of the EDC in bold blue in Fig. 6(a) is plotted in Fig. 6(b). This shows in more detail a large and sharp peak in the quasiparticle density of states at E_F as expected from the flat band near E_F and associated sharp peak in the density of states identified in the band structure calculations. We speculate that the anomalous c-axis thermal expansion behavior and perhaps some of the magnetic properties we observe for $SrCo_2As_2$ are driven by the presence of this flat band at or near E_F.

In general, this Fermi surface (FS) is very different from those of other related parent compounds of the 122 family like $BaFe_2As_2$ and $SrFe_2As_2$, where the hole FSs at Γ and the electron FSs at X are roughly circular in shape and similar in size.[53] To gain more insight about the character of the FS pockets, in Figs. 5(b) and 5(c) we show the energy-momentum ARPES intensity maps along two different cuts, marked by the white [across the Γ (0,0) point] and black [across the X $(\pi/a, -\pi/a)$ point] bars in Fig. 5(a). In Fig. 5(b), one can

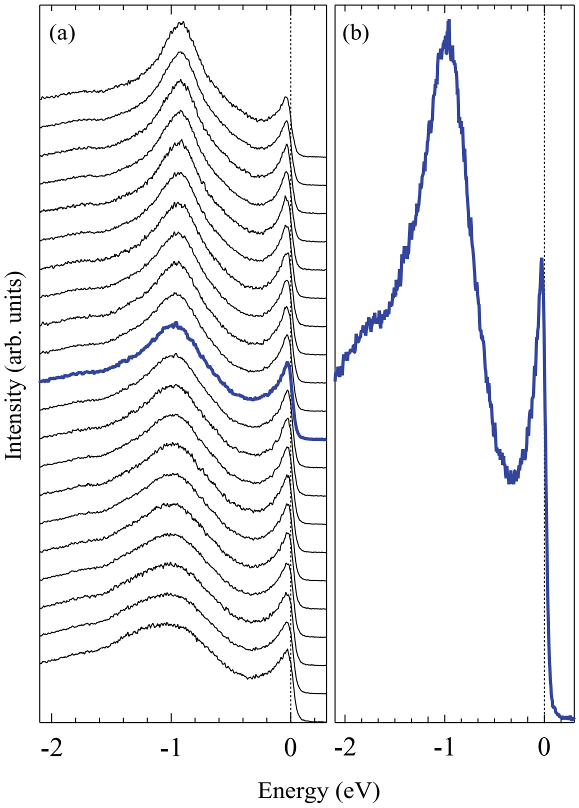

FIG. 6. (Color online) (a) Energy distribution curves (EDCs) at fixed wave vector as the wave vector is scanned through the Γ point along the white bar at the top of Fig. 5(c), which is from $k_\alpha = 0.52\,\pi/a$ to $1.19\,\pi/a$. The EDC highlighted in bold blue is at $k_\alpha = 0.85\,\pi/a$. The Fermi energy E_F is at the zero of energy on the horizontal scale. (b) Enlargement of the EDC at $k_\alpha = 0.85\,\pi/a$ that is plotted in bold blue in (a). The sharp quasiparticle peak near E_F arises from a flat electron band with a sharp peak in the density of states near E_F.

observe a rather weak but discernible electron-like FS pocket at the Γ point and two additional small electron pockets at $\pm\pi/a$. A general observation in $\mathrm{Ba(Fe_{1-x}Co_x)_2As_2}$ is that with increasing x (electron doping), the central hole pockets at Γ become electron-like, while the X pockets remain electron-like and keep expanding on the overdoped side of the phase diagram (see, e.g., the ARPES data for the $x = 0.42$ sample in Ref. 54). An electron pocket at the center of the BZ [Fig. 5(b)] for $\mathrm{SrCo_2As_2}$ is expected and is in overall agreement with our previous study of $\mathrm{Ba(Fe_{1-x}Co_x)_2As_2}$.[54] The pocket at the X point is also electron-like, but much larger in size [Fig. 5(c)], so there is no obvious Fermi surface nesting in $\mathrm{SrCo_2As_2}$.

We extracted the Fermi momenta of the electron pockets from the peaks in the momentum distribution curves at E_F (not shown), and were found to be about ± 0.2 Å^{-1} [vertical black arrows at the top of Fig. 5(b)] and ± 0.7 Å^{-1} [vertical black arrows at the top of Fig. 5(c)] centered at the Γ and X points, respectively. Figure 5(b) also shows that the top of the hole band at the Γ point has moved from above E_F for the $A\mathrm{Fe_2As_2}$ compounds to about 400 meV below E_F due to Co contributing one conduction electron more than Fe. This leads to the disappearance of the hole-like Fermi surface around the Γ point as discussed above[54] and is consistent with our recent ARPES study of $\mathrm{BaCo_2As_2}$.[55] In particular, the energies of the top and bottom of the valence band at the Γ and X points, the size of the electron pockets surrounding the Γ point, and the location and extent of the flat band at the X point are very similar for both materials.

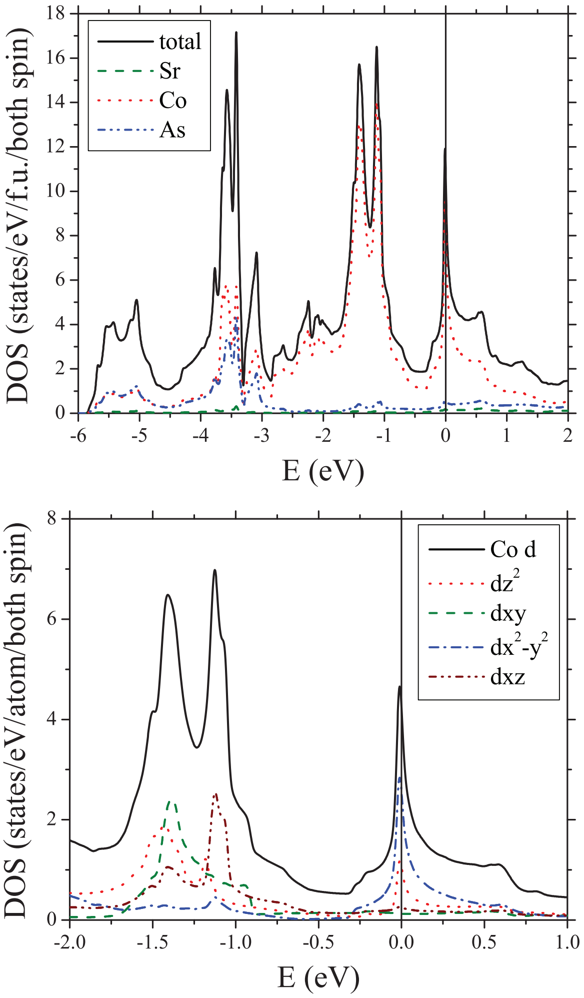

FIG. 7. (Color online) (Top panel) Total and atom-decomposed density of states (DOS) of $\mathrm{SrCo_2As_2}$ versus energy E. (Bottom panel) Orbital-decomposed contributions of the Co $3d$ atoms to the DOS. The peak in the total DOS near $E_\mathrm{F} = 0$ is mostly contributed by the Co atoms. The DOS shows three peaks in the energy range shown. The peak near E_F is mainly from the $d_{x^2-y^2}$ flat-band component, and the second peak near 1.2 eV below E_F is from the d_{xz}, d_{yz} components, which are degenerate in tetragonal symmetry. The third peak near 1.5 eV below E_F is from the d_{xy} and d_{z^2} components. The ordinate scales of the DOS are different in the two panels because the top panel is for all atoms whereas the bottom panel is for the Co atoms separately.

VI. BAND STRUCTURE CALCULATIONS

The top and bottom panels of Fig. 7 are atom- and orbital-decomposed densities of states (DOS), which were calculated with 1631 **k** points in the irreducible BZ. The top panel shows strongly hybridized bonding states between Co and As atoms in the energy range from 3 to 6 eV below E_F. There are also antibonding empty states but they are located outside of the energy range shown. It also shows, near E_F, a strong peak,

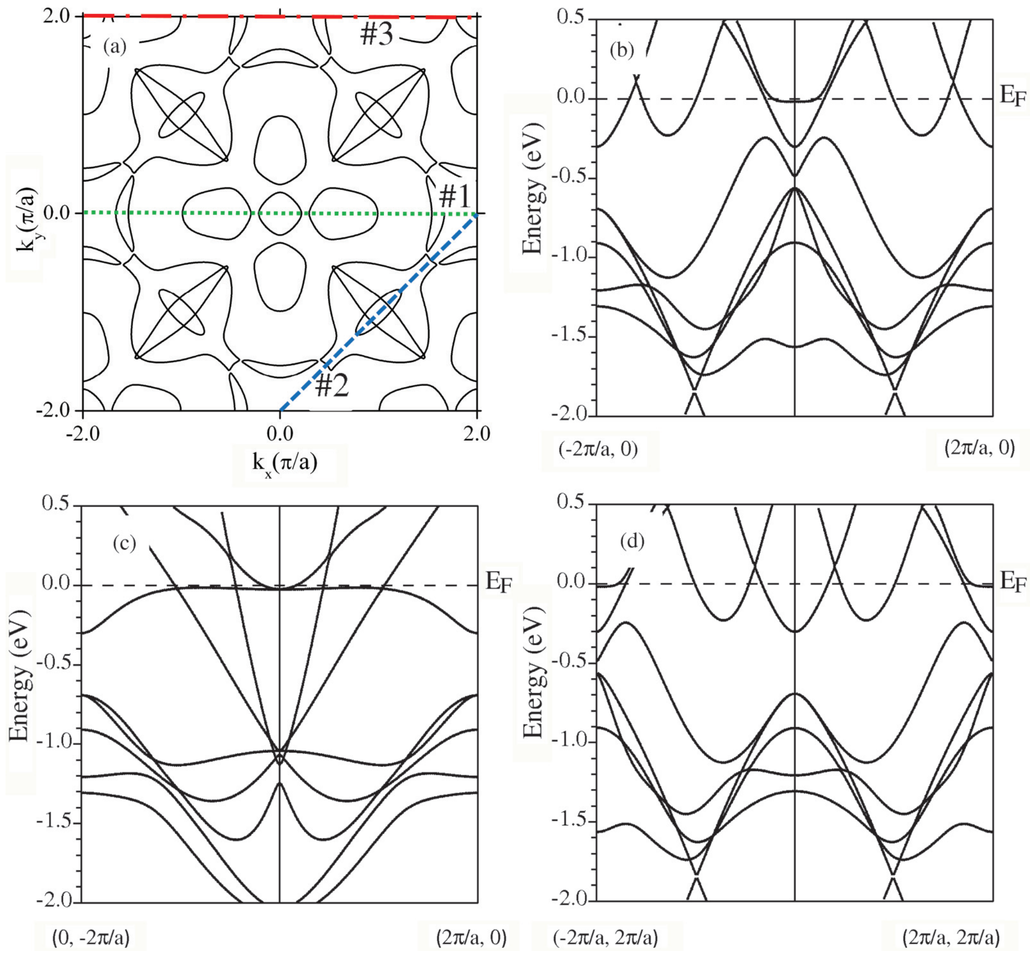

FIG. 8. (Color online) Plots of (a) the Fermi surface and (b)–(d) the band structure of $SrCo_2As_2$ calculated at $k_z = 1.88(\pi/c)$. The lines (#1–#3) in (a) are cutting lines for band structure plot directions and correspond to panels (b)–(d), respectively. The lattice parameters a and c are those of the body-centered tetragonal unit cell of $SrCo_2As_2$ given in Sec. II.

which is mostly of Co d character. It is well known that a system that has a high DOS or peak at E_F is unstable and has a tendency to split the peak (lower the total energy) via physical transformations such as magnetic or structural transitions.[56] Therefore it might be expected that $SrCo_2As_2$ also shows peculiar temperature- or pressure-dependent properties, which depend on the precise peak position.

The bottom panel of Fig. 7 shows the orbital-decomposed Co atom DOS in a small energy range (from 2 eV below to 1 eV above E_F) to emphasize the orbital contributions to the peak near E_F. The $d_{x^2-y^2}$ orbital points towards neighboring Co atoms in the xy plane and is a dominant contributor, where the x and y axes are defined here to be along the a and b axes of the Co square lattice, respectively. It suggests a possibility to control the peak size or position by Co–Co distance modification.

Thus the very sharp peak in the DOS near E_F in Fig. 7(a) arises from a Co $d_{x^2-y^2}$ flat band extending over a large fraction of the second BZ. The band structure density of states at E_F is

$$\mathcal{D}^{\text{band}}(E_F) = 11.04 \text{ states/(eV f.u.) both spins.} \qquad (2)$$

Figure 8 shows a Fermi surface (FS) plot and band structures for three different cuts in **k** space. For the Fermi surface calculation, we divided the $-2\pi/a < k_x, k_y < 2\pi/a$ range of k_x,k_y planes with different k_z values into a 200×200 mesh that gives 40401 **k** points. Figure 8(a) shows the result with $k_z = 1.88(\pi/c)$ and also shows three cutting lines for band structure calculations. The cutting line #1 is from $(-2\pi/a,0,z)$ to $(2\pi/a,0,z)$, #2 is from $(0,-2\pi/a,z)$ to $(2\pi/a,0,z)$, and cutting line #3 is from $(-2\pi/a,2\pi/a,z)$ to $(2\pi/a,2\pi/a,z)$, with $z = 1.88(\pi/c)$. These cutting lines #1–#3 correspond to the band structure plots Figs. 8(b)–8(d), respectively. Figure 8(c) shows the $d_{x^2-y^2}$ flat band that is largely responsible for the sharp high peak in the DOS near E_F.

VII. HEAT CAPACITY

The C_p of $SrCo_2As_2$ is plotted versus T in Fig. 9. The value of C_p at 240 K is 124 J/mol K, which is close to the Dulong-Petit high-T limit of the lattice heat capacity at constant volume given by $C_V = 15R \approx 124.7$ J/mol K, where R is the molar gas constant. The inset in Fig. 9 shows a conventional C_p/T versus T^2 plot for $T \leqslant 10$ K where the data are fitted by the expression

$$C_p/T = \gamma + \beta T^2 + \delta T^4, \qquad (3)$$

which is the sum of electronic (γT) and low-T lattice ($\beta T^3 + \delta T^5$) heat capacity contributions. The fitted values of

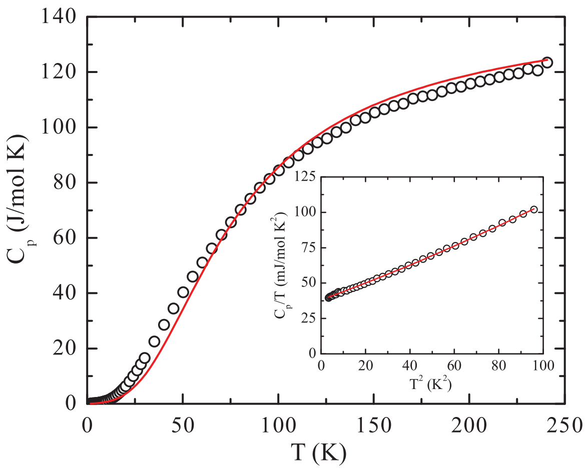

FIG. 9. (Color online) Heat capacity C_p versus temperature T for $SrCo_2As_2$. The red curve is a fit by Eqs. (9). Inset: C_p/T versus T^2. The curve is a fit by Eq. (3).

the Sommerfeld coefficient γ and the lattice coefficients β and δ are listed in Table II. The value of $\gamma = 37.8(1)$ mJ/mol K^2 is very large compared to those of the parent iron arsenide compounds AFe_2As_2 (A = Ca, Sr, Ba) in the stripe AFM state.[57–59] Additional $C_p(T)$ data at $H = 3$ T down to 1.3 K revealed no new features (not shown).

TABLE II. Parameters derived from $C_p(T)$, $\rho(T)$, and χ data of ACo_2As_2 (A = Sr, Ba). The listed parameters are the Sommerfeld coefficient γ and the coefficients β and δ of the lattice heat capacity at low T in Eq. (3), density of states at the Fermi energy obtained from $T \to 0$ heat capacity $\mathcal{D}^{\gamma}(E_F)$ and magnetic susceptibility $\mathcal{D}^{\chi}(E_F)$ measurements, respectively, Wilson ratio $R_W = \mathcal{D}^{\chi}(E_F)/\mathcal{D}^{\gamma}(E_F)$, density of states at the Fermi energy obtained from band structure calculations $\mathcal{D}^{\rm band}(E_F)$, Debye temperatures Θ_D and Θ_R determined from heat capacity and resistivity measurements, respectively, coefficient A of the T^2 term in ρ at low T, Kadowaki-Woods ratio $R_{KW} = A/\gamma^2$, electron-phonon coupling constant $\lambda_{\text{el-ph}}$ and the electronic many-body mass enhancement $m^*/m_{\rm band}$. The β value for $BaCo_2As_2$ was calculated by digitizing the C_p/T versus T^2 data in Ref. 24.

Parameter	$SrCo_2As_2$ (This work)	$BaCo_2As_2$ (Refs. 24 and 63)
γ (mJ/mol K^2)	37.8(1)	41.0
β (mJ/mol K^4)	0.611(7)	0.47
δ (μJ/mol K^6)	1.01(9)	
$\mathcal{D}^{\gamma}(E_F)$[a]	16.0(3)	17.4
$\mathcal{D}^{\chi}(E_F)$[a]	54	90
R_W	3.4	5.2
$\mathcal{D}^{\rm band}(E_F)$[a]	11.04	8.5
Θ_D (K) (Low T)	251(1)	274
Θ_D (K) (All T)	304(3)	
Θ_R (K) (All T)	167(1)	
A (10^{-3} $\mu\Omega$ cm/K^2)	7.92(3)	2.2
R_{KW}[b]	5.7	1.3
$(1 + \lambda_{\text{el-ph}})m^*/m_{\rm band}$	1.45	2.0

[a] The units are states/(eV f.u.) for both spin directions.
[b] The units are 10^{-3} mΩ cm mol^2 J^{-2} K^2.

The density of states at the Fermi energy for both spin directions $\mathcal{D}(E_F)$, including many-body enhancement effects due to the electron-phonon and electron-electron interactions, is calculated from

$$\gamma = \frac{\pi^2 k_B^2}{3}\mathcal{D}^{\gamma}(E_F). \tag{4}$$

Using the above value of γ yields

$$\mathcal{D}^{\gamma}(E_F) = 16.0(3)\ \text{states/eV f.u.} \tag{5}$$

for both spin directions. This value is 1.45 times the band theory value of 11.04 states/(eV f.u.) (see Table II). Writing $\gamma = \gamma_{\rm band}(1 + \lambda_{\text{el-ph}})m^*/m_{\rm band}$, where $\gamma_{\rm band}$ and $m_{\rm band}$ are the band theory values of γ and the current carrier effective mass, $\lambda_{\text{el-ph}}$ is the electron-phonon coupling constant and $m^*/m_{\rm band}$ is the electronic many-body conduction carrier mass enhancement over the band theory value, gives

$$(1 + \lambda_{\text{el-ph}})m^*/m_{\rm band} \approx 1.45. \tag{6}$$

A similar analysis of γ obtained at low T has been done for paramagnetic $BaCo_2As_2$, where the authors find[24]

$$\gamma = 41.0\ \text{mJ/mol K}^2, \tag{7a}$$

$$\mathcal{D}^{\gamma}(E_F) = 17.4\ \text{states/eV f.u.}, \tag{7b}$$

$$(1 + \lambda_{\text{el-ph}})m^*/m_{\rm band} \approx 2.0. \tag{7c}$$

The γ and $\mathcal{D}^{\gamma}(E_F)$ values of $SrCo_2As_2$ and $BaCo_2As_2$, respectively, are seen to be nearly the same. The difference between the combined electron-phonon and electronic mass enhancements in Eqs. (6) and (7c) arises mainly from the difference in the band structure densities of states of the two compounds.

The Debye temperature Θ_D is obtained from the value of β according to

$$\Theta_D = \left(\frac{12\pi^4 Rn}{5\beta}\right)^{1/3}, \tag{8}$$

where β is normalized to a mole of formula units (f.u.) and $n = 5$ is the number of atoms per f.u. Thus we obtain $\Theta_D = 251(1)$ K. This value is much larger than the value $\Theta_R = 167(1)$ K obtained above in Sec. IV from the Bloch-Grüneisen fit to $\rho(T)$. This discrepancy may be associated with the unusual negative thermal expansion characteristics discussed in Sec. III B above and/or with T-dependent spin fluctuation effects discussed in Sec. IX below and associated magnetoelastic coupling effects.

The Kadowaki-Woods (KW) ratio is $R_{KW} = A/\gamma^2 = 5.7 \times 10^{-3}$ mΩ cm mol^2 J^{-2} K^2, similar to those observed in strongly-correlated electron metals and heavy fermion compounds,[60] thus suggesting the presence of strong electron correlations in $SrCo_2As_2$.

The $C_p(T)$ data in the entire T range of measurement were fitted by

$$C_p(T) = \gamma T + nC_{\rm V\,Debye}(T), \tag{9a}$$

where γ was fixed at the above-determined value 37.8 mJ/mol K^2 and $n = 5$ is the number of atoms/f.u. The function $C_{\rm V\,Debye}(T)$ is the Debye lattice heat capacity at constant volume per mole of atoms due to acoustic phonons given by[61]

$$C_{\rm V\,Debye}(T) = 9R\left(\frac{T}{\Theta_D}\right)^3 \int_0^{\Theta_D/T} \frac{x^4 e^x}{(e^x - 1)^2}\, dx, \tag{9b}$$

where Θ_D is the Debye temperature. A high-accuracy analytic Padé approximant[48] for the Debye function in Eq. (9b) was used for fitting the $C_p(T)$ data, which greatly facilitates the fit. The Θ_D derived from the least-squares fit of the data over the full T range in Fig. 9 by Eq. (9a) is 304(3) K as listed in Table II. This value of Θ_D is significantly larger than the value of 251(1) K determined above from fitting the C_p data at low $T < 10$ K by Eq. (3). Furthermore, the goodness of fit obtained is poor, evident from the large systematic deviations of the fit from the data in Fig. 9 compared to the much better fits we recently obtained for other 122-type compounds.[27,48] This unusually large deviation between the two Θ_D values might be related to the negative thermal expansion reported in Sec. III B and/or magnetoelastic coupling effects arising from strongly T-dependent spin fluctuations. The parameters of the above fits and derived quantities are summarized in Table II.

VIII. MAGNETIZATION AND MAGNETIC SUSCEPTIBILITY

The isothermal magnetization M of a $SrCo_2As_2$ single crystal versus H for $H \parallel c$ and $H \parallel ab$ plane are shown in Figs. 10(a) and 10(b), respectively. The M is proportional to H for the entire T and H ranges of the measurements for both field directions, showing that the crystal does not contain detectable ferromagnetic (FM) or saturable PM impurities. Therefore the susceptibility can be defined at arbitrary field H as $\chi = M(H)/H$.

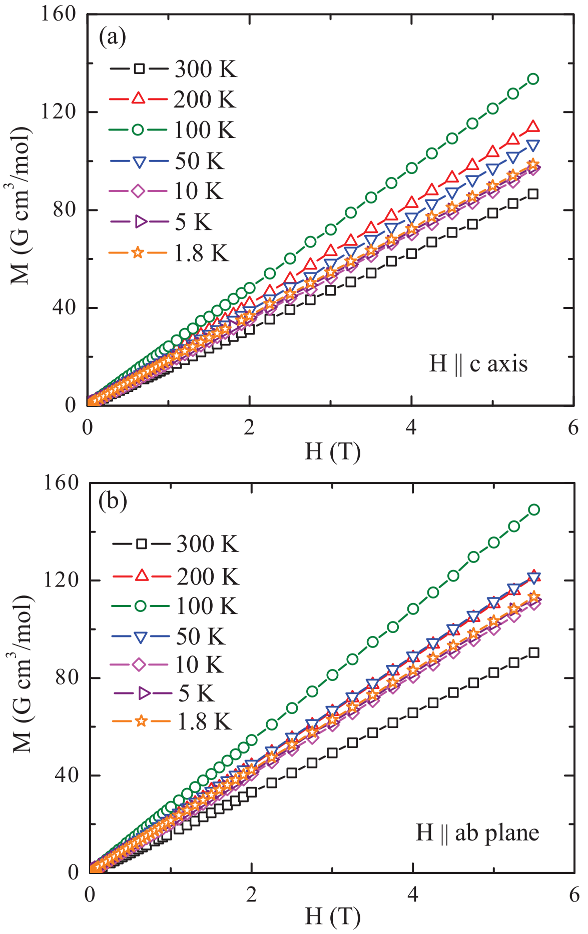

FIG. 10. (Color online) Isothermal magnetization M of $SrCo_2As_2$ versus applied magnetic field H at the indicated temperatures for H parallel to (a) the c axis and (b) the ab plane.

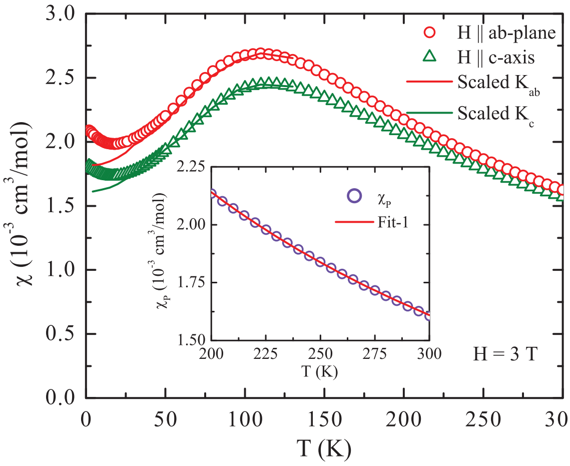

FIG. 11. (Color online) Anisotropic magnetic susceptibility $\chi \equiv M/H$ versus temperature T (where M is magnetization and H is applied magnetic field) of $SrCo_2As_2$ measured at $H = 3$ T. From our NMR Knight shift measurements in Fig. 16(a) below, the upturns in $\chi(T)$ below about 20 K are not intrinsic. The solid curves are these Knight shift data scaled onto the low-T $\chi(T)$ data, allowing estimates of the intrinsic $\chi(T \to 0)$ values to be obtained as given in Eq. (10). Inset: Fit of the powder-averaged susceptibility χ_P versus T for $200\text{ K} \leqslant T \leqslant 300$ K by the Curie-Weiss law in Eq. (20) with $\chi_0 \equiv 0$ (Fit 1 in Table III). Fits 1 and 2 are indistinguishable on the scale of the inset.

The anisotropic magnetic susceptibilities χ_{ab} and χ_c of $SrCo_2As_2$ in $H = 3$ T are plotted versus T in Fig. 11, where $\chi_c \equiv \chi(H \parallel c)$ and $\chi_{ab} \equiv \chi(H \parallel ab \text{ plane})$. The $\chi(T)$ data for both field directions exhibit broad maxima at ≈ 115 K followed by shallow minima at ≈ 20 K and smooth low-T upturns below 20 K, with no evidence for long-range magnetic ordering. A very similar broad maximum in χ at about the same temperature was observed for isostructural KFe_2As_2.[62] The maximum in $\chi(T)$ for that compound was attributed to a crossover from a coherent to an incoherent Fermi liquid state with increasing T.[62]

The T dependences of the ^{75}As NMR Knight shift $K(T)$ data in Fig. 16(a) below are in overall agreement with the $\chi(T)$ data in Fig. 11, except that the $K(T)$ data do not show the upturns seen in the $\chi(T)$ data below ≈ 20 K. This difference indicates that these upturns in $\chi(T)$ are not intrinsic and therefore likely arise from paramagnetic impurities or defects that are not saturable in our field range (see Fig. 10). The Knight shift data from Fig. 16(a) are therefore scaled onto the respective low-T $\chi(T)$ data in Fig. 11 as shown by the solid curves, which represent the intrinsic $\chi(T)$ at low T. The intrinsic values for $SrCo_2As_2$ at 4.3 K are found to be

$$\chi_c(0) = 1.61 \times 10^{-3}\ \text{cm}^3/\text{mol}, \tag{10a}$$

$$\chi_{ab}(0) = 1.82 \times 10^{-3}\ \text{cm}^3/\text{mol}, \tag{10b}$$

$$\chi_P(0) = 1.75 \times 10^{-3}\ \text{cm}^3/\text{mol}, \tag{10c}$$

where the powder-averaged susceptibility χ_P is

$$\chi_P = \tfrac{1}{3}\chi_c + \tfrac{2}{3}\chi_{ab}. \tag{10d}$$

The effective density of states at E_F for both spin directions $\mathcal{D}^{\chi}(E_F)$ obtained from magnetic susceptibility measurements is calculated from $\chi_P(0)$ for $g = 2$ using the expression

$$\chi_P(0) = \mu_B^2 \mathcal{D}^{\chi}(E_F), \tag{11}$$

yielding a large density of states

$$\mathcal{D}^{\chi}(E_F) = 54 \text{ states/(eV f.u.)}. \tag{12}$$

The anisotropy in χ is small with $\chi_{ab}(0)$ slightly larger than $\chi_c(0)$. The sign of the anisotropy is opposite to that in the PM state of $CaCo_2As_2$ (Refs. 25 and 26) and in $BaCo_2As_2$.[24,63]

For comparison, from the high-field slopes from 2 to 6.5 T of the $M(H)$ data for $BaCo_2As_2$ at $T = 1.8$ K in the inset of Fig. 1 of Ref. 24, we obtain[63]

$$\chi_c(0) = 3.28 \times 10^{-3} \text{ cm}^3\text{/mol}, \tag{13a}$$

$$\chi_{ab}(0) = 2.72 \times 10^{-3} \text{ cm}^3\text{/mol } (BaCo_2As_2), \tag{13b}$$

$$\chi_P(0) = 2.91 \times 10^{-3} \text{ cm}^3\text{/mol}. \tag{13c}$$

These values are $\sim 70\%$ larger than our respective values at 4.3 K for $SrCo_2As_2$ in Eq. (10). The density of states calculated from $\chi_P(0)$ for $BaCo_2As_2$ using Eq. (11) is

$$\mathcal{D}^{\chi}(E_F) = 90 \text{ states/(eV f.u.)} \quad (BaCo_2As_2). \tag{14}$$

A. Stoner enhancement and the Wilson ratio: a conundrum

In an itinerant picture, the Stoner-enhanced susceptibility at $\mathbf{q} = 0$ and $T = 0$ is[64]

$$\chi = \frac{\chi_0}{1 - \mathcal{D}_{\text{band}}(E_F)I/4} \equiv \frac{\chi_0}{1 - F}, \tag{15}$$

where χ_0 is the conduction carrier spin susceptibility calculated from the band-structure density of states at E_F as in Eq. (11), $I \sim 0.8$ eV is the Stoner factor for Co (Ref. 24) and the factor of 1/4 arises due to the presence of two Co atoms per f.u. and from the two spin directions counted in $\mathcal{D}(E_F)$. Using $\mathcal{D}_{\text{band}}(E_F) = 11.04$ states/(eV f.u.) from Eq. (2) and $I = 0.8$ eV gives

$$F = 2.2 > 1, \tag{16}$$

which from comparison with Eq. (15) indicates that $SrCo_2As_2$ should have a FM ground state. This inference is wrong because it strongly disagrees with our $M(H)$ and $\chi(T)$ data in Figs. 10 and 11, respectively.

The Wilson ratio R_W is defined as

$$R_W \equiv \frac{\mathcal{D}^{\chi}(E_F)}{\mathcal{D}^{\gamma}(E_F)}. \tag{17}$$

Within an itinerant picture, if $R_W \sim 1$–2, χ and γ are approximately equally enhanced above the band structure prediction, indicating that any enhancement of χ and γ is due to a many-body enhancement of $\mathcal{D}(E_F)$. On the other hand, if $R_W \gg 1$ or $R_W \ll 1$, one would infer that strong FM or AFM conduction spin correlations are present, respectively, which change χ but not γ.[65] Using the values of $\mathcal{D}^{\chi}(E_F)$ and $\mathcal{D}^{\gamma}(E_F)$ in Eqs. (12) and (5), respectively, Eq. (17) gives

$$R_W = 3.5 \quad \text{for} \quad SrCo_2As_2. \tag{18}$$

As discussed above, this large value of R_W indicates a significant FM enhancement of χ, qualitatively consistent with the large value of the factor F derived above.

These indications of dominant FM correlations between the itinerant current carriers in $SrCo_2As_2$ are at odds with the broad maximum in $\chi(T)$ at about 115 K in Fig. 11, which instead suggests the dominance of low-dimensional AFM correlations,[7] and with the linear $M(H)$ behaviors in Fig. 10 that show no tendency towards saturation. Indeed, inelastic neutron scattering measurements on this compound showed strong AFM fluctuations at the stripe AFM wave vector,[23] but preliminary searches for FM spin fluctuations in the first BZ yielded no detectable signal. On the other hand, electronic structure calculations of the static $\chi(\mathbf{q})$ showed enhancements at both the FM and stripe AFM wave vectors.[23] Interestingly, enhancements of $\chi(\mathbf{q})$ at the same two wave vectors are found from electronic structure calculations and χ measurements of the FeAs-based materials.[3,11]

A similar analysis of χ and C_p data for isostructural $BaCo_2As_2$ yielded a similar conclusion about the importance of FM itinerant spin correlations in this compound.[24] Using the densities of states for $BaCo_2As_2$ in Eqs. (7b) and (14), one obtains the value of the Wilson ratio from Eq. (17) as

$$R_W = 5.2 \quad \text{for} \quad BaCo_2As_2. \tag{19}$$

This value is larger than for $SrCo_2As_2$ in Eq. (18), suggesting stronger FM correlations in this compound. The authors of Ref. 24 suggested that the suppression of long-range FM order in $BaCo_2As_2$ results from strong spin fluctuations associated with a nearby quantum critical point.

B. Curie-Weiss model

Above ≈ 200 K, the $\chi(T)$ of $SrCo_2As_2$ resembles a Curie-Weiss-like (CW) behavior

$$\chi = \chi_0 + \frac{C}{T - \theta_p}. \tag{20}$$

The values of the Curie constant C and Weiss temperature θ_p obtained by fitting $\chi_P(T)$ between 200 and 300 K, assuming $\chi_0 = 0$ (Fit 1), are listed in Table III. In a second fit, the χ_0 value was allowed to vary, yielding a different set of fit parameters (Fit 2) in Table III. Fit 1 is shown as the red curve in the inset of Fig. 11; both fits to the data are equally good and cannot be distinguished on the scale of the inset. In a local-moment

TABLE III. Parameters derived from fitting the powder-averaged magnetic susceptibility $\chi_P(T)$ in the T range 200 K $\leqslant T \leqslant$ 300 K by the Curie-Weiss law (20). The error bars reflect systematic errors found by varying the temperature range of the fits. The g factor and effective moment μ_{eff} are calculated using Eqs. (21) and (22), respectively, assuming spin $S = 1/2$.

Parameter	Fit 1	Fit 2
χ_0 (10^{-4}cm^3/mol)	$\equiv 0$	$-4(2)$
C (cm^3 K/mol)	0.65(1)	1.0(2)
g	1.86(2)	2.3(2)
$\mu_{\text{eff}}(\mu_B/\text{Co})$	1.61(2)	2.0(2)
θ_p (K)	$-102(7)$	$-180(50)$

model, the Curie constant per mole of spins is given by

$$C = \frac{N_A g^2 S(S+1)\mu_B^2}{3k_B}, \tag{21}$$

where N_A is Avogadro's number, g is the spectroscopic splitting factor (g factor), S is the spin quantum number, μ_B is the Bohr magneton, and k_B is Boltzmann's constant. The corresponding effective magnetic moment is computed from

$$\mu_{\rm eff} = g\sqrt{S(S+1)}\,\mu_B/\text{Co}. \tag{22}$$

The calculated values of g and $\mu_{\rm eff}$ for the two fits taking $S = 1/2$ are given in Table III.

For an interacting local moment Heisenberg model $\mathcal{H} = \sum_{\langle ij\rangle} J_{ij}\mathbf{S}_i \cdot \mathbf{S}_j$ for identical crystallographically equivalent spins, one has[66]

$$\theta_p = -\frac{S(S+1)}{3k_B}\sum_j J_{ij}, \tag{23}$$

where the sum is over all interacting neighbors j of a given spin i. Within the J_1-J_2 model for the square Co lattice where J_1 and J_2 are the four nearest- and four next-nearest-neighbor exchange interactions, respectively, and using $S = 1/2$, one obtains

$$\theta_p = -\frac{J_1 + J_2}{k_B}. \tag{24}$$

Our θ_p values then give

$$\frac{J_1 + J_2}{k_B} = 102(7)\ \text{K} \quad \text{(Fit 1)}, \tag{25a}$$

$$\frac{J_1 + J_2}{k_B} = 180(50)\ \text{K} \quad \text{(Fit 2)}, \tag{25b}$$

which are strongly antiferromagnetic. We emphasize that the values of C, $\mu_{\rm eff}$, θ_p, and $J_1 + J_2$ may be in error because the CW fit to the $\chi(T)$ data may not have been done at sufficiently high temperatures for the CW law to accurately describe the data, and/or because $SrCo_2As_2$ may be an itinerant magnetic system instead of a local-moment one.

The results of $\chi(T)$ measurements on a polycrystalline $SrCo_2As_2$ sample were reported earlier by Leithe-Jasper *et al.*[18] The authors found that $SrCo_2As_2$ is a CW paramagnet showing no magnetic ordering above 1.8 K with $C = 0.53$ cm^3 K/mol and $\theta_p = -29$ K. These C and $|\theta_p|$ values are both significantly smaller than our values in Table III for a single crystal, and these authors did not report observing the maximum in $\chi(T)$ that we observe at ≈ 115 K in Fig. 11 for both field orientations and therefore which also occurs for the polycrystalline average.

C. Interconfigurational fluctuation (ICF) model

As discussed above, in an itinerant picture one expects $SrCo_2As_2$ and $BaCo_2As_2$ to be ferromagnetic. The observed absence of ferromagnetism in these compounds suggests that strong spin fluctuation effects prevent the occurrence of long-range FM ordering, perhaps due to proximity to a quantum critical point.[24] The observed broad maximum in $\chi(T)$ in Fig. 11 and the large magnitude of θ_p in Table III can then be analyzed within a phenomenological interconfigurational fluctuation (ICF) model where the average fluctuating valence of the magnetic ions in a material is T-dependent.[67,68] For this model, at high T we find a CW-like $\chi(T)$ with a negative (AFM-like) Weiss temperature, as observed, which conflicts with the positive (FM-like) Weiss temperature expected if $SrCo_2As_2$ were near a FM instability. A many-body theory of intermediate-valence and interconfigurational fluctuation effects[69] has been applied to understand the T-dependent local moment[70] and associated anomalous T dependence of χ (Ref. 3) in the PM states of the iron arsenides.

The ICF model is derived from the χ of an isolated two-level local-moment magnetic system. Here we apply it to local-moment d-electron systems with quenched orbital angular momentum ($L_z = 0$). Spin-orbit coupling generally causes a deviation of g from the free-electron value $g = 2$ and the introduction of a paramagnetic Van Vleck orbital susceptibility. The ground state has energy $E_0 \equiv 0$, spin S_0, and Zeeman degeneracy $2S_0 + 1$, and the excited state has energy E_1, spin S_1, and degeneracy $2S_1 + 1$. The spin susceptibility of this two-level system is then

$$\chi_{\text{two-level}}(T) = P_0\chi_0(T) + P_1\chi_1(T), \tag{26a}$$

where the probabilities of occupying state 0 or 1 are given by the Boltzmann distribution as

$$P_i = \frac{(2S_i + 1)e^{-E_i/k_BT}}{(2S_0 + 1) + (2S_1 + 1)e^{-E_1/k_BT}} \quad (i = 0,1). \tag{26b}$$

The susceptibilities of the two levels are given by Curie laws as

$$\chi_i(T) = \frac{C_i}{T} \quad (i = 0,1) \tag{26c}$$

with Curie constants

$$C_i = \frac{N_A g_i^2 S_i(S_i + 1)\mu_B^2}{3k_B} \quad (i = 0,1). \tag{26d}$$

The phenomenological ICF susceptibility $\chi_{\rm ICF}$ is derived from the above results for an isolated two-level system by making the replacement

$$T \to T^\star \tag{27a}$$

in Eqs. (26), where[68]

$$T^\star = \sqrt{T^2 + T_{\rm sf}^2} \quad \text{(model 1)} \tag{27b}$$

or[67]

$$T^\star = T + T_{\rm sf} \quad \text{(model 2)} \tag{27c}$$

and $T_{\rm sf}$ is an effective spin fluctuation temperature that reflects the frequency of fluctuations in the spin state of the magnetic ion between S_0 and S_1.

We fitted our experimental $\chi(T)$ by

$$\chi(T) = \chi_0 + \chi_{\rm ICF}(T), \tag{28}$$

where χ_0 is the T-independent orbital susceptibility and $\chi_{\rm ICF}$ is the ICF spin susceptibility. We tried the combinations $(S_0,S_1) = (0,\frac{1}{2})$, $(0,1)$, $(0,\frac{3}{2})$, $(\frac{1}{2},1)$, and $(1,\frac{3}{2})$, but only the combination $(S_0,S_1) = (0,1)$ gave a satisfactory fit to the experimental data, for which Eqs. (26) and (27) yield

$$P_1(T) = \frac{3}{3 + e^{E_1/k_BT^\star}} \quad (S_0 = 0,\ S_1 = 1) \tag{29a}$$

TABLE IV. Parameters obtained from fitting the powder-averaged susceptibility $\chi_{\rm P}(T)$ of SrCo$_2$As$_2$ using the phenomenological interconfigurational flutuation (ICF) model. The fitted parameters are the energy of the excited triplet states E_1, spin fluctuation temperature $T_{\rm sf}$, temperature independent contribution to the magnetic susceptibility χ_0, and spectroscopic splitting factor g_1 for the excited-state Zeeman levels. Parameters derived from these are the Curie constant C_1 for the excited triplet levels, the Curie constant $C_{\rm ICF}$, and Weiss temperature $\theta_{\rm ICF}$ for the Curie-Weiss-like susceptibility in Eq. (29f) followed at high T in the ICF model.

Model	$E_1/k_{\rm B}$ (K)	$T_{\rm sf}$ (K)	χ_0 (10^{-3} cm^3/mol)	g_1	C_1 (cm^3 K/mol)	$C_{\rm ICF}$ (cm^3 K/mol)	$\theta_{\rm ICF}$ (K)
Model 1	224(1)	83.7(7)	−0.85(1)	2.25(5)	1.26	0.95	−56
Model 2	468(5)	183(3)	−4.29(6)	4.8(2)	5.76	4.32	−300

and, using $\chi_0(T) = 0$ because $S_0 = 0$,

$$\chi_{\rm ICF}(T) = \frac{3C_1}{(3 + e^{E_1/k_{\rm B}T^\star})T^\star} \quad (S_0 = 0,\ S_1 = 1). \tag{29b}$$

Using the expression for $T^\star$ for model 1 in Eqs. (27), a high-T series expansion of Eq. (29b) gives

$$\chi_{\rm ICF}(T) = \frac{C_{\rm ICF}}{T}\left[1 - \frac{E_1/k_{\rm B}}{4T} - \frac{(E_1/k_{\rm B})^2 + 8T_{\rm sf}^2}{16T^2} + \mathcal{O}\left(\frac{1}{T^3}\right)\right], \tag{29c}$$

where

$$C_{\rm ICF} = \frac{3C_1}{4} \tag{29d}$$

and $T_{\rm sf}$ first appears in the third term. The factor of $3/4$ arises because in the limit of high T the probability of occupying the triplet excited state is $3/4$. In this limit, Eq. (29c) yields a Curie law

$$\chi_{\rm ICF}(T) = \frac{C_{\rm ICF}}{T}, \tag{29e}$$

where $C_{\rm ICF}$ is the Curie constant of the two-level system at high T. Expanding the first two terms in Eq. (29c) in a Taylor series according to $1 + x \approx 1/(1 - x)$ gives a Curie-Weiss-like behavior

$$\chi_{\rm ICF}(T) = \frac{C_{\rm ICF}}{T - \theta_{\rm ICF}} \quad (T \gg \theta_{\rm ICF}), \tag{29f}$$

where the Weiss temperature is

$$\theta_{\rm ICF} = -\frac{E_1}{4k_{\rm B}} \quad \text{(model 1)} \tag{30a}$$

with a negative sign (AFM-like). It is interesting that this expression for $\theta_{\rm ICF}$ in model 1 does not contain the ICF parameter $T_{\rm sf}$. Carrying out the same steps for model 2 gives a Curie-Weiss law (29f) with the same Curie constant but a different Weiss temperature

$$\theta_{\rm ICF} = -\left(\frac{E_1}{4k_{\rm B}} + T_{\rm sf}\right) \quad \text{(model 2)}, \tag{30b}$$

which for this model does contain $T_{\rm sf}$.

The values of the fitted parameters χ_0, E_1, $T_{\rm sf}$, and g_1 for models 1 and 2 using $(S_0, S_1) = (0, 1)$ are listed in Table IV and the fits by the two models are shown in Fig. 12. Also listed in Table IV are the values of C_1, $C_{\rm ICF}$, and $\theta_{\rm ICF}$ derived from these parameters using Eqs. (26d), (29d), and (30), respectively. Although good fits are obtained using both models, the χ_0 value for the fit by model 2 is unphysically large and negative and even the value for model 1 is unusually negative. Furthermore, the values of $C_{\rm ICF}$ and $\theta_{\rm ICF}$ are much closer to the Curie-Weiss fit values in Table III for model 1 compared to model 2. However, we only expect the fitting parameters to be semiquantitative because the ICF model is phenomenological.

Figure 13 shows the T dependence of the fractional population P_1 of the magnetic excited triplet state with $S_1 = 1$

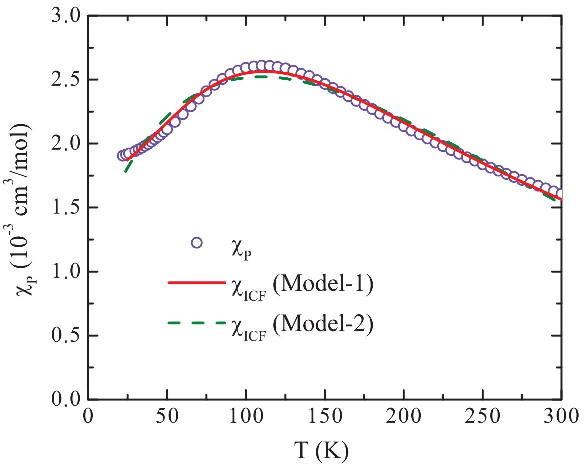

FIG. 12. (Color online) Powder averaged susceptibility $\chi_{\rm P}$ versus T of SrCo$_2$As$_2$ along with the fit using the two different interconfigurational fluctuation models in Eqs. (27).

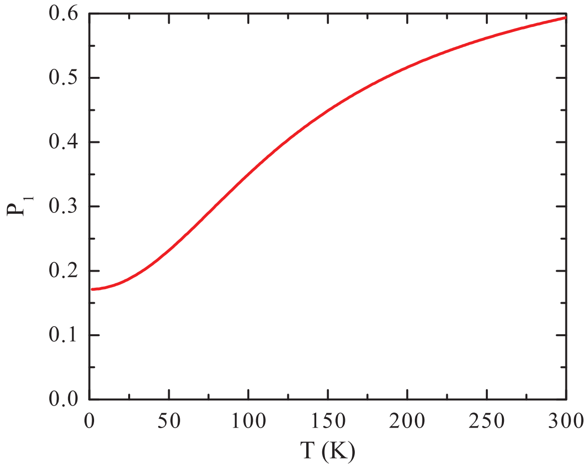

FIG. 13. (Color online) Temperature T dependence of the fractional population P_1 of the excited magnetic state with spin $S_1 = 1$ for model 1 in Eqs. (26), (27), and (29a).

for model 1 and the parameters in Table IV. Our thermal expansion measurements in Fig. 3(a) show that $\mathrm{SrCo_2As_2}$ exhibits anomalous negative thermal expansion along the c direction and positive thermal expansion in the basal plane, which results in a a/c ratio that is T dependent and increases with increasing T with a dependence similar to that in Fig. 13 [see Fig. 3(c)]. Thus the T dependence of a/c and the population $P_1(T)$ are correlated within this model.

D. J_1-J_2 Heisenberg model with $S = 1/2$

1. *Introduction*

It is well known that low-dimensional Heisenberg antiferromagnets exhibit a $\chi(T)$ that has a broad maximum due to the increasing dynamic short-range AFM correlations on cooling below the temperature of the maximum, in conjunction with the suppression of long-range AFM order due to quantum fluctuations associated with the low spin-lattice dimensionality.[7] In view of the inelastic neutron scattering results that demonstrated the occurrence of dynamic stripe-type AFM correlations in $\mathrm{SrCo_2As_2}$,[23] we consider in this section a description of our $\chi(T)$ data in Fig. 11, which show a broad maximum, in terms of the J_1-J_2 Heisenberg model for the two-dimensional (2D) spin-1/2 square lattice. Due to the Mermin-Wagner theorem,[71] a 2D Heisenberg spin lattice cannot exhibit static long-range AFM order at finite T. This result is due to fluctuation affects associated with the low dimensionality of the spin lattice. However, even weak interlayer coupling can induce long-range AFM order, but usually at a temperature significantly below the temperature of the broad peak in $\chi(T)$.[72]

The J_1-J_2 Heisenberg model with spins $S = 1/2$ on a square lattice is well studied. The Hamiltonian in zero field is

$$\mathcal{H} = \sum_{\langle ij\rangle} J_1 \mathbf{S}_i \cdot \mathbf{S}_j + \sum_{\langle ik\rangle} J_2 \mathbf{S}_i \cdot \mathbf{S}_j, \tag{31}$$

where the first sum is over nearest-neighbor spin pairs along the legs of the square lattice and the second sum is over next-nearest-neighbor spin pairs along the diagonals of the squares, where positive J_1 and J_2 correspond to AFM interactions and negative ones to FM interactions. A stripe-type AFM phase as observed in the LaFeAsO and $A\mathrm{Fe_2As_2}$ compounds occurs classically for $J_2 > 0$ and $J_2/|J_1| > 1/2$, where J_1 can be either positive (AFM) or negative (FM).[3] Early in the Fe-based high-T_c superconductivity field, this (effective) frustration model was used to explain the stripe-type AFM ordering observed in the 1111-type and 122-type iron arsenides in both the itinerant[73] and local moment[74] descriptions of the magnetism. The same stripe-type AFM ordering is predicted from band theory without reference to exchange interactions.[11,12]

Our recent inelastic neutron scattering measurements on $\mathrm{SrCo_2As_2}$ indicate the presence of stripe-type AFM correlations with $J_1 < 0$ and $J_2/J_1 \approx -1$,[23] which is consistent with the above classical constraints for stripe-type AFM correlations, and further indicated that the correlations are quasi-two-dimensional. We therefore proceed to analyze our $\chi(T)$ data for $\mathrm{SrCo_2As_2}$ in terms of the frustrated 2D J_1-J_2 spin-1/2 Heisenberg square lattice model.

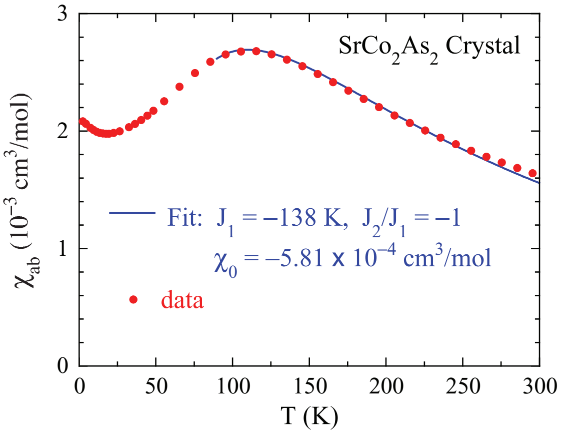

FIG. 14. (Color online) A fit of the ab-plane susceptibility $\chi_{ab}(T)$ data for $\mathrm{SrCo_2As_2}$ from Fig. 11 (filled red circles) by the J_1-J_2 spin-1/2 Heisenberg model on a square lattice according to Eq. (33) (blue curve). The fitting parameters are given in the figure where $g = 2$ was assumed.

2. *Determining J_1 and J_2 from $\chi(T)$ data*

In order to estimate the values of the exchange constants J_1 and J_2, one can fit $\chi(T)$ by the high-T series expansion (HTSE) for the spin susceptibility of this model which is given for $J_1 < 0$ and $J_2 > 0$ by[75]

$$\frac{\chi|J_1|}{Ng^2\mu_{\mathrm{B}}^2} = \frac{|J_1|}{k_{\mathrm{B}}T}\sum_{n=0}^{9}\left(\frac{-|J_1|}{k_{\mathrm{B}}T}\right)^n \sum_{m=0}^{n} c_{m,n}\left(\frac{J_2}{J_1}\right)^m, \tag{32}$$

where N is the number of spins and a table of the $c_{m,n}$ values is given in Ref. 75. For a given value of J_2/J_1, we converted the sum over n into a Padé approximant $\mathcal{P}[p,q]$ with $[p,q] = [4,4]$, which is a ratio of two fourth-order polynomials in $|J_1|/k_{\mathrm{B}}T$ ($p = q = 4$), where the coefficients of the two polynomials are solved for exactly in terms of the original HTSE coefficients, which in turn results in an expression $\chi_{\mathrm{Pade}}(T)$ for the susceptibility. The Padé approximant reformulation of the HTSE prediction for χ decreases the minimum temperature at which the HTSE can be used to fit experimental data.

We fitted our $\chi(T)$ data by

$$\chi(T) = \chi_0 + \chi_{\mathrm{Pade}}(T,|J_1|,J_2/J_1). \tag{33}$$

A fit of the experimental $\chi_{ab}(T)$ data in Fig. 11 by Eq. (33) for $J_1 < 0$ and $J_2/J_1 = -1$ was obtained, as dictated by the inelastic neutron scattering measurements,[23] and we also fixed $g = 2$. The fit is shown in Fig. 14, where the fitting parameters χ_0 and J_1 are given in the figure. The high-temperature series and Padé approximant derived from it are not expected to be valid to temperatures much below the temperature of the broad maximum, so we cut off the fit as shown. The value of χ_0 is perhaps too negative to be physical, which suggests that the model may not include all relevant exchange couplings.

3. *Extended 3D J_1-J_2-J_c spin $S = 1/2$ Heisenberg model*

The above fit of $\chi(T)$ by the J_1-J_2 model ignores the magnetic coupling between adjacent stacked Co square lattice layers along the c axis. To include this coupling, we utilize the above intralayer $\chi_{\mathrm{Pade}}(T)$ in Eq. (33) as determined from Eq. (32), but augment the J_1-J_2 Heisenberg square lattice model by adding a nearest-neighbor c-axis Heisenberg coupling between the stacked square lattices using molecular field theory (MFT) as follows, where we utilize the fact that all Co spins are identical and crystallographically equivalent in $\mathrm{SrCo_2As_2}$.

The time- and space-average magnetic moment component μ_i in the direction of the applied field $\mathbf{H}$ is

$$\mu_i = \frac{\chi_{\rm Pade}}{N}(H + H_{{\rm exch}\,c\,i}), \tag{34a}$$

where $H_{{\rm exch}\,c\,i}$ is the exchange field seen by $\vec{\mu}_i$ due to the two moments in the two adjacent layers along the c axis. In MFT, one writes

$$H_{{\rm exch}\,c\,i} = \lambda_c \mu_i, \tag{34b}$$

where λ_c is the MFT coupling constant of $\vec{\mu}_i$ to the two moments in adjacent layers along the c axis. Substituting Eq. (34b) into (34a) and solving for μ_i gives

$$\mu_i = \frac{\frac{\chi_{\rm Pade}}{N}H}{1 - \frac{\chi_{\rm Pade}}{N}\lambda_c}, \tag{34c}$$

so the spin susceptibility per spin is

$$\chi_i^{\rm spin} = \frac{\mu_i}{H} = \frac{\chi_{\rm Pade}/N}{1 - \frac{\chi_{\rm Pade}}{N}\lambda_c}, \tag{34d}$$

and for N spins one then obtains

$$\chi^{\rm spin} = \frac{\chi_{\rm Pade}}{1 - \frac{\chi_{\rm Pade}}{N}\lambda_c}. \tag{34e}$$

Taking the reciprocal of each side of this equation gives

$$\frac{1}{\chi^{\rm spin}} = \frac{1}{\chi_{\rm Pade}} - \frac{\lambda_c}{N}. \tag{34f}$$

Thus the MFT coupling parameter λ_c just shifts the entire inverse susceptibility versus T curve vertically by an amount $-\lambda_c/N$, and therefore does not change the temperature of the maximum in $\chi(T)$ at about 115 K in Fig. 14.

Now we express λ_c in terms of an exchange constant J_c between a spin and a nearest-neighbor spin in an adjacent layer. The part of the Heisenberg Hamiltonian associated with the interaction of spin $\mathbf{S}_i$ with the two nearest-neighbor spins $\mathbf{S}_j$ in adjacent layers is

$$\mathcal{H}_i = \frac{1}{2}J_c\mathbf{S}_i \cdot \sum_{j=1}^{2}\mathbf{S}_j = \frac{J_c}{2g^2\mu_{\rm B}^2}\vec{\mu}_i \cdot \sum_{j=1}^{2}\vec{\mu}_j, \tag{35}$$

where the factor of 1/2 arises because the exchange energy is equally shared by each spin within a pair of interacting spins. The magnetic moment $\vec{\mu}$ and spin $\mathbf{S}$ vectors are related by $\vec{\mu} = -g\mathbf{S}\mu_{\rm B}$, where the minus sign arises from the negative sign of the charge on the electron. In MFT, one writes the time- and space-average of the energy per spin E_i in the PM state as

$$E_i = \frac{J_c}{g^2\mu_{\rm B}^2}\mu_i\mu_j \equiv -\frac{1}{2}\mu_i H_{{\rm exch}\,c\,i}, \tag{36}$$

where the factor of 1/2 on the right-hand side arises because when calculating the exchange field, all of the interaction energy E_i between moments $\vec{\mu}_i$ and $\vec{\mu}_j$ is assigned to the neighbor $\vec{\mu}_j$ of $\vec{\mu}_i$. Then, recognizing that the average moments satisfy $\mu_i = \mu_j$ in the PM state, the exchange field associated with the c-axis interactions is found from Eq. (36) to be

$$H_{{\rm exch}\,c\,i} = -\frac{2J_c}{g^2\mu_{\rm B}^2}\mu_i. \tag{37}$$

Comparing Eqs. (37) and (34b) gives λ_c in terms of J_c as

$$\lambda_c = -\frac{2J_c}{g^2\mu_{\rm B}^2}. \tag{38}$$

Substituting Eq. (38) into (34e) gives

$$\chi^{\rm spin}(T) = \frac{\chi_{\rm Pade}(T)}{1 + \frac{2J_c\chi_{\rm Pade}(T)}{Ng^2\mu_{\rm B}^2}}. \tag{39}$$

From Eq. (39), an AFM (positive) J_c suppresses the susceptibility, whereas a FM (negative) J_c enhances it, as expected. Our inelastic neutron scattering results indicated an AFM Co-Co interlayer interaction in $\mathrm{SrCo_2As_2}$.[23] Therefore the anomalously negative value of χ_0 derived in the previous section that suppresses χ probably arises at least in part from the presence of the c-axis AFM Co-Co interactions that are neglected in the J_1-J_2 model. Using Eq. (39), in order to produce the same effect on $\chi(T)$ at its maximum as $\chi_0 = -5.8 \times 10^{-4}\ \mathrm{cm^3/mol}$ (Fig. 14) would require $J_c/k_{\rm B} = 460$ K, which according to our inelastic neutron scattering data (Ref. 23) is much too large compared to $|J_1|$, $J_2 = 138$ K and should therefore be considered an upper limit. We conclude that within the present model, a significant diamagnetic χ_0 value as well as a significant AFM c-axis coupling are present.

Finally, we add a caveat that our analyses of the magnetic properties of AFM $\mathrm{CaCo_2As_2}$ indicate that the magnetism is itinerant,[27] whereas the above analyses of $\chi(T)$ for $\mathrm{SrCo_2As_2}$ were carried out within a local-moment picture.

IX. NMR SPECTROSCOPY

Figure 15 shows field-swept ^{75}As-NMR spectra of $\mathrm{SrCo_2As_2}$ at $T = 4.2$ K for two magnetic field directions of $H \parallel c$ axis and $H \parallel ab$ plane. The spectra exhibit features

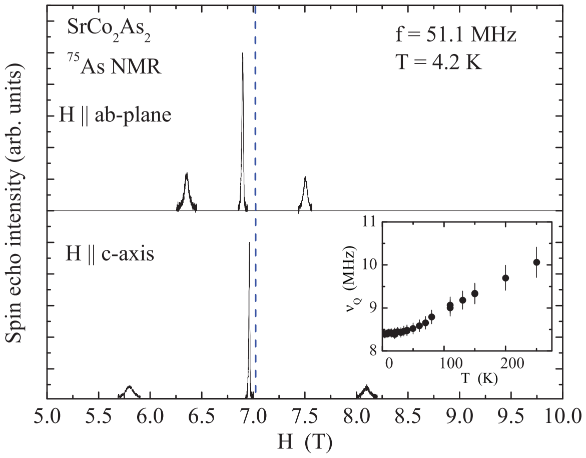

FIG. 15. (Color online) Field-swept ^{75}As-NMR spectra of $\mathrm{SrCo_2As_2}$ at temperature $T = 4.2$ K for magnetic fields H perpendicular and parallel to the c axis. The vertical dashed blue line corresponds to the zero-shift ($K = 0$) position. Inset: ^{75}As nuclear quadruple frequency $\nu_{\rm Q}$ versus T.

typical of a nuclear spin $I = 3/2$ with Zeeman and quadrupolar interactions, which result in a sharp central transition and two satellite peaks split by the quadrupolar interaction of the ^{75}As nucleus with the local electric field gradient (EFG). The principle axis of the EFG at the As site in tetragonal $\mathrm{SrCo_2As_2}$ is found to be along the crystal c axis as for members of the $A\mathrm{Fe_2As_2}$ family that have tetragonal symmetry,[76–80] since in our CoAs-based compound and in the tetragonal FeAs-based materials the As site has a local fourfold rotational symmetry about the c axis. The spectra for $\mathrm{SrCo_2As_2}$ for both H directions did not show any obvious magnetic broadenings at any temperature between 1.6 and 275 K, which indicates that static magnetic ordering does not occur in this compound above 1.6 K.

The inset of Fig. 15 shows the temperature dependence of the nuclear quadrupole frequency $\nu_\mathrm{Q} = eQV_{ZZ}/2h$, where Q is the electric quadrupole moment of the ^{75}As nucleus, V_{ZZ} is the principal-axis EFG at the As site and h is Planck's constant. V_{ZZ} arises from hybridization between the As-4p and Co-3d orbitals with an additional contribution from the noncubic part of the spatial distribution of surrounding ions. The ν_Q decreases by about 15% on cooling, from 10 MHz at 250 K to 8.45 MHz at 1.6 K. A decrease of ν_Q by $\sim 15\%$ on lowering T from 280 to 140 K was also observed in $\mathrm{BaFe_2As_2}$ (Ref. 76) where ν_Q is much smaller in $\mathrm{BaFe_2As_2}$ than in $\mathrm{SrCo_2As_2}$. These behaviors sharply contrast with that observed for $\mathrm{SrFe_2As_2}$ where ν_Q *increases* from 2.0 MHz at 300 K to 2.6 MHz at ~ 210 K.[76]

Figure 16(a) shows the T dependences of the NMR shifts K_{ab} and K_c for H parallel to the ab plane and parallel to the c axis, respectively, where the second-order quadrupole shift was corrected for in $K_{ab}(T)$. As T decreases below room temperature, both K_{ab} and K_c increase and show broad maxima at the about the same temperature of ≈ 115 K, similar to the $\chi(T)$ behavior in Fig. 11, and then decrease monotonically at lower T without showing upturns. The small upturns in $\chi(T)$ observed at low T in Fig. 11 are therefore not intrinsic and evidently arise from a small amount of a PM impurity that is not saturable in fields up to 5.5 T (see Fig. 10).

Figure 16(b) shows K_{ab} and K_c from Fig. 16(a) versus χ_{ab} and χ_c from Fig. 11, respectively, with T as an implicit parameter, for $T > 35$ K to avoid the extrinsic low-temperature upturns in $\chi(T)$. Both K_{ab} and K_c vary linearly with the corresponding χ and, from the respective slopes, the hyperfine coupling constants are estimated to be $A_{ab} = (65.9 \pm 2.8)$ kOe/μ_B and $A_c = (45.0 \pm 1.0)$ kOe/μ_B, respectively. These values are much larger than $A_{ab} = 29.3$ kOe/μ_B and $A_c = 20.4$ kOe/μ_B for $\mathrm{SrFe_2As_2}$, respectively.[76] Since the hyperfine coupling is mainly due to hybridization between the 4s and 4p orbitals of the As atoms with the 3d orbitals of the Co atoms, the large hyperfine couplings indicate a strong hybridization between these orbitals. This is consistent with the large ν_Q for ^{75}As in $\mathrm{SrCo_2As_2}$ because the ν_Q is also affected by the strength of the hybridization between the As-4p and Co-3d orbitals. The y intercepts of the respective linear fits of K versus χ in Fig. 16(b) are nearly zero. This indicates that the NMR shifts originate mainly from the spin susceptibility with almost negligible net contribution from the orbital (chemical) paramagnetic Van Vleck and diamagnetic conduction electron Landau susceptibilities. Therefore, we identify the measured NMR shifts as Knight shifts.

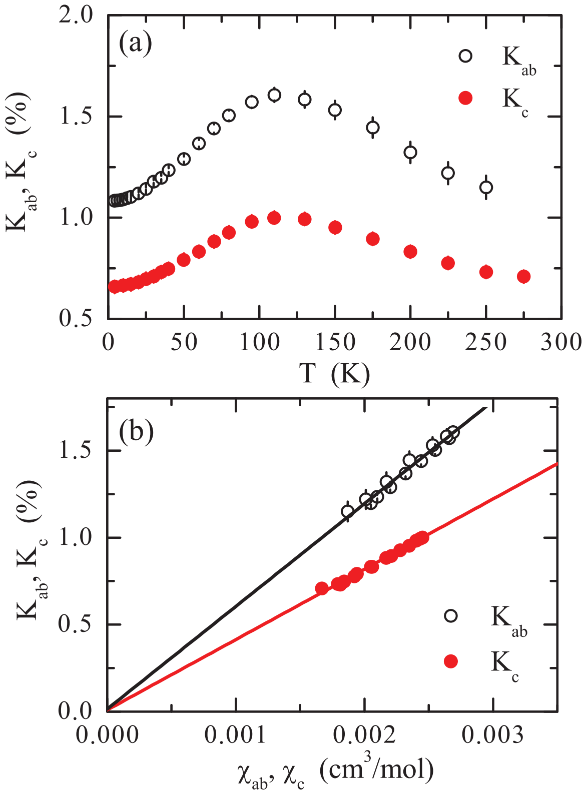

FIG. 16. (Color online) (a) Temperature T dependence of the ^{75}As NMR shifts K_{ab} and K_c for $\mathrm{SrCo_2As_2}$. (b) K vs χ plots for the corresponding ab and c components of K and χ with T as an implicit parameter for 35 K $\leqslant T \leqslant$ 275 K. The linear fits are not forced to go through the origin; however, the fitted y intercepts are almost zero, as shown.

The ^{75}As nuclear spin-lattice relaxation rate $1/T_1$ at each T is determined by fitting the nuclear magnetization M versus time t dependence of the central line after saturation using the double-exponential function $1 - M(t)/M(\infty) = 0.1\exp(-t/T_1) + 0.9\exp(-6t/T_1)$ as expected for the central line of the spectrum of the ^{75}As ($I = 3/2$) nucleus, where $M(t)$ and $M(\infty)$ are the nuclear magnetization at time t after saturation and the equilibrium nuclear magnetization at $t \to \infty$, respectively. Figure 17(a) shows $1/T_1$ versus T for magnetic fields parallel and perpendicular to the c axis. Both $1/T_1$ measurements show very similar T dependencies, which consist of a weak T dependence at high temperatures above ~ 150 K followed by a monotonic decrease at lower T.

Within a Fermi liquid picture, $1/T_1T$ is proportional to the square of the density of states at the Fermi energy $\mathcal{D}(E_\mathrm{F})$. On the other hand, the Knight shift is proportional to the Pauli spin susceptibility $\chi^\mathrm{Pauli} = \mu_\mathrm{B}^2\mathcal{D}(E_\mathrm{F})$. By looking at the behavior of T_1TK^2 versus T, one can therefore test the applicability of the Fermi liquid theory to our system which predicts the Korringa relation T_1TK^2 = const. As shown in Fig. 17(b), T_1TK^2 for both H directions are indeed nearly independent of T for $\mathrm{SrCo_2As_2}$. This means that the conduction carriers form a Fermi liquid. The T^2 dependence of $\rho(T)$ observed

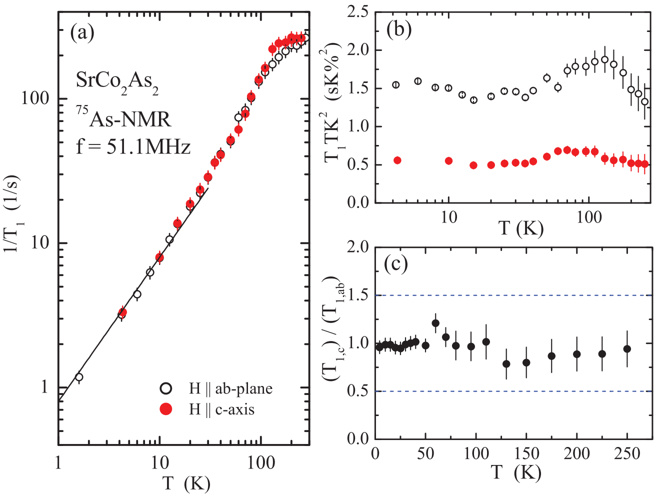

FIG. 17. (Color online) (a) Temperature dependence of $1/T_1$ for SrCo$_2$As$_2$ for both magnetic field directions, $H \parallel c$ axis and $H \parallel ab$ plane. The straight line shows the metallic Korringa dependence $1/T_1 \propto T$. (b) T dependence of T_1TK^2. The symbol designations are the same as in (a). (c) T dependence of the ratio $r \equiv T_{1,c}/T_{1,ab}$.

below 38 K in the inset of Fig. 4 above is another indication of Fermi liquid behavior.

Next, we discuss the relationship between the anisotropy of our $1/T_1$ data and the anisotropy of the Co spin fluctuations. Here we follow the same procedure previously performed on Fe pnictides.[76,81,82] In general, $1/T_1$ can be described in terms of the fluctuating hyperfine field perpendicular to the applied magnetic field at the NMR angular frequency $\omega_{\rm N}$ according to

$$\begin{aligned}\left(\frac{1}{T_1}\right)_z &= \frac{\gamma_{\rm N}^2}{2}\int_{-\infty}^{\infty}[\langle H_{{\rm hf},x}(t),H_{{\rm hf},x}(0)\rangle \\ &\quad + \langle H_{{\rm hf},y}(t),H_{{\rm hf},y}(0)\rangle]\exp(i\omega_{\rm N}t)\,dt \\ &= \gamma_{\rm N}^2\sum_{\mathbf{q}}[|H_{{\rm hf},x}(\mathbf{q},\omega_{\rm N})|^2 + |H_{{\rm hf},y}(\mathbf{q},\omega_{\rm N})|^2], \end{aligned} \quad (40)$$

where the z direction corresponds to the external field direction and $|X(\mathbf{q},\omega_{\rm N})|^2$ denotes the $\mathbf{q}$-dependent power spectral density at $\omega_{\rm N}$ of a time-dependent random variable $X(t)$.

Defining the hyperfine coupling tensor as $\tilde{A}$, the hyperfine fields at the As site can be described as the sum of contributions from the four nearest-neighbor Co spins as[77,82]

$$\mathbf{H}_{\rm hf}(\mathbf{q},\omega_{\rm N}) = \sum_{i=1}^{4}\tilde{A}_i\mathbf{S}_i(\mathbf{q},\omega_{\rm N}) = \tilde{A}\mathbf{S}_i(\mathbf{q},\omega_{\rm N}), \quad (41)$$

where

$$\tilde{A} = \begin{pmatrix} A_a & D & B_1 \\ D & A_b & B_2 \\ B_1 & B_2 & A_c \end{pmatrix}. \quad (42)$$

Here, $\tilde{A}$ is described in orthorhombic axis (stacked Co square-lattice) notation for consistency with the previous discussion on Fe pnictides.[77] We consider the cases where A_α ($\alpha = a, b, c$), B_i ($i = 1,2$) and D in $\tilde{A}$ are, respectively, the diagonal components along the α direction with $\mathbf{q} = (0,0)$, the off-diagonal components related to stripe AFM correlations with $\mathbf{q} = (\pi,0)$ or $(0,\pi)$, and the off-diagonal components associated with Néel-type spin correlations with $\mathbf{q} = (\pi,\pi)$.[81] Defining the amplitude of the spin fluctuation spectral density as $\mathcal{S}_\alpha \equiv \sqrt{|S_\alpha(\mathbf{q},\omega_{\rm N})|^2}$ ($\alpha = a,\ b,\ c$), using the above equations and writing $A_{ab} \equiv A_a = A_b$ and $\mathcal{S}_{ab} \equiv \mathcal{S}_a = \mathcal{S}_b$ appropriate to the tetragonal symmetry of SrCo$_2$As$_2$, the ratio

$$r \equiv \frac{T_{1,c}}{T_{1,ab}} \quad (43)$$

is obtained as[82]

$$r = \begin{cases} 0.5 + 0.5\left(\frac{A_c\mathcal{S}_c}{A_{ab}\mathcal{S}_{ab}}\right)^2 & \text{for } \mathbf{q} = (0,0), \quad (44a) \\ 0.5 + \left(\frac{\mathcal{S}_{ab}}{\mathcal{S}_c}\right)^2 & \text{for } \mathbf{q} = (\pi,0) \text{ or } (0,\pi), \quad (44b) \\ 0.5 & \text{for } \mathbf{q} = (\pi,\pi). \quad (44c) \end{cases}$$

As plotted in Fig. 17(c), r is almost constant versus T with a value $r \approx 1$. From our inelastic neutron scattering measurements, the dominant AFM fluctuations/correlations are stripe-type with $\mathbf{q} = (\pi,0)$ or $(0,\pi)$ in Co square-lattice notation.[23] According to Eq. (44b), the value $r \approx 1$ observed in Fig. 17(c) then arises from anisotropic spin fluctuations with $\mathcal{S}_{ab} \approx 0.71\,\mathcal{S}_c$. This means that stripe-type AFM Co spin fluctuations along the c-axis are stronger than in the ab plane. An anisotropy in spin fluctuations is also observed in various Fe-based superconductors in the paramagnetic state near $T_{\rm N}$, but $\mathcal{S}_{ab}$ is always larger than $\mathcal{S}_c$,[76,83] in contrast to our result for SrCo$_2$As$_2$. Néel-type AFM spin fluctuations with $\mathbf{q} = (\pi,\pi)$ can be ruled out because according to Eq. (44c), that would require $r = 0.5$ in conflict with our measurements in Fig. 17(c) that give $r \approx 1$.

Our $1/T_1$ data can also be analyzed with Eq. (44a) solely in terms of FM spin fluctuations with $\mathbf{q} = (0,0)$. Using the ratio of the hyperfine fields $A_c/A_{ab} = 45.0/65.9 = 0.653$ determined from the K-χ plot in Fig. 16(b), $r \approx 1$ can be reproduced with anisotropic spin fluctuations with $\mathcal{S}_{ab} = 0.65\,\mathcal{S}_c$. Interestingly, this analysis also gives the same nature of the anisotropy of the spin fluctuations as discussed above for stripe-type AFM fluctuations. Therefore one cannot uniquely determine the nature of the spin fluctuations utilizing NMR data alone. The $\mathbf{q}$-dependent static susceptibility $\chi(\mathbf{q})$ obtained from electronic structure calculations showed a peak at $\mathbf{q} = (0,0)$ as well as at $\mathbf{q} = (\pi,0)$ and $(0,\pi)$,[23] so spin fluctuations may well occur with peaks at both the FM and stripe-type AFM wave vectors.

From our NMR data on SrCo$_2$As$_2$ crystals we conclude that the conduction carriers form a Fermi liquid that exhibits significant FM and/or AFM spin fluctuations. The presence of strong AFM spin fluctuations at low temperatures has been specifically demonstrated from our inelastic neutron scattering measurements of single crystals,[23] and FM correlations from the strongly enhanced χ discussed above in Sec. VIII A.

X. SINGLE-CRYSTAL NEUTRON DIFFRACTION

The above thermal expansion, $\rho(T)$, $C_{\rm p}(T)$, $\chi(T)$, and NMR measurements showed no evidence for any phase transitions from 1.3 to 300 K in SrCo$_2$As$_2$. This result is consistent with the neutron scattering measurements on SrCo$_2$As$_2$ crystals[23] that showed no evidence for long-range AFM order at the propagation vector of the stripe-type AFM order found[3] in the 122-type iron arsenides. However, the

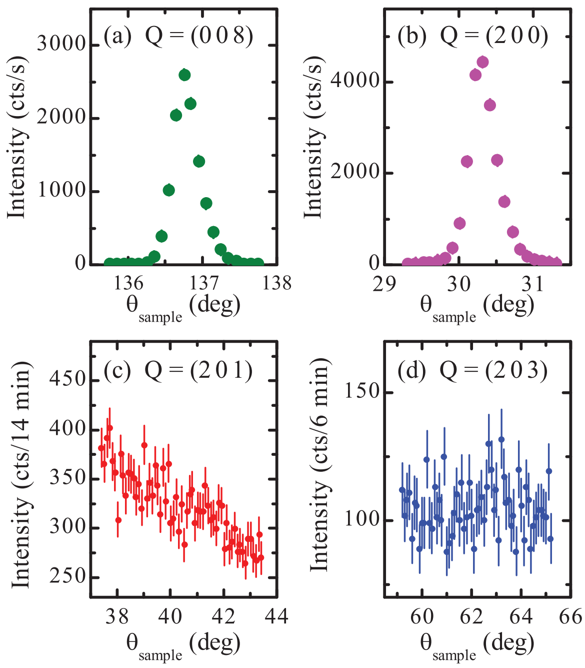

FIG. 18. (Color online) Single-crystal neutron diffraction measurements at $T = 3$ K searching for A-type AFM order in $\mathrm{SrCo_2As_2}$. The (0 0 8) and (2 0 0) nuclear Bragg peaks are shown in panels (a) and (b), respectively. The neutron intensity measured as the sample is rocked through the (2 0 1) and (2 0 3) positions at which magnetic Bragg peaks would be observed for A-type AFM ordering is shown in panels (c) and (d), respectively. The calculated values of $\theta_{\rm sample}$ of this potential type of AFM ordering are 40.4° in (c) and 62.2° in (d), respectively, which are near the middle of the respective scans.

inelastic neutron scattering measurements did show strong dynamic AFM correlations in $\mathrm{SrCo_2As_2}$ at this propagation vector.[23] On the other hand, neutron diffraction measurements on $\mathrm{CaCo_2As_2}$ confirmed the presence of A-type long-range AFM order characterized by magnetic Bragg peaks at reciprocal lattice points (h 0 ℓ) with $h + \ell = 2n + 1$ [e.g., (2 0 1) and (2 0 3)] with an upper limit of 0.6 $\mu_{\rm B}$/Co for the ordered moment.[27]

To complement the above null result for the occurrence of long-range stripe-type AFM ordering in $\mathrm{SrCo_2As_2}$, here we searched for evidence of A-type[27] or G-type[41] long-range AFM order in a $\mathrm{SrCo_2As_2}$ crystal using single-crystal neutron diffraction at the base temperature of $T \approx 3$ K and did not find any such evidence. Figure 18 shows scans through both nuclear [Figs. 18(a) and 18(b)] and A-type AFM [Figs. 18(c) and 18(d)] Bragg peak positions. There is no evidence of scattering above background at the latter positions. Note the factor of ~15,000 finer scale of the ordinates for the potential AFM peak positions in Figs. 18(c) and 18(d) compared to those of the nuclear reflections in Figs. 18(a) and 18(b). The small increase in scattering with decreasing angle in Fig. 18(c) is likely due to some degree of preferred orientation in the Al sample can since the scattering angle is close to that for the Al (2 0 0) powder line. Measurements to check for G-type long-range AFM order are complicated by the fact that the AFM Bragg reflections are coincident with nuclear Bragg peaks. However, we found no evidence of enhanced scattering at the (1 0 1) position of the strongest G-type AFM reflection (not shown).

XI. GROUND STATE OF $\mathrm{SrCo_2As_2}$

Our x-ray and neutron diffraction, $\rho(T)$, $M(H,T)$, $\chi(T)$, $C_{\rm p}(T)$, and NMR measurements reveal no evidence for any phase transitions in $\mathrm{SrCo_2As_2}$ from 300 K down to 1.3 K. On the other hand, the temperature $T_{\max} \approx 115$ K at which the broad maximum in $\chi(T)$ occurs, the Weiss temperature $\theta_{\rm p} \sim -150$ K in the Curie-Weiss law fits from 200 to 300 K in Table III, the large values of $|J_1| = J_2 = 138$ K in Fig. 14 obtained by fitting the $\chi(T)$ data by the J_1-J_2 model, and the observation of strong stripe-type AFM spin correlations in neutron scattering measurements[23] demonstrate that AFM spin correlations are present and are strong. However, long-range AFM order is not observed above 1.3 K. A measure of the ratio of the energy scale of the AFM spin correlations to the long-range AFM transition temperature $T_{\rm N} < 1.3$ K is therefore

$$f = \frac{|\theta_{\rm p}|}{T_{\rm N}} \gtrsim 100. \tag{45}$$

In insulating local-moment systems, f is called the frustration parameter.[84] In such systems in which frustration prevents long-range AFM ordering, a ratio $f \gtrsim 100$ and the absence of static magnetic ordering of any kind occurring in the accessible temperature range point towards a quantum spin-liquid (QSL) ground state in which quantum fluctuations prevent static long-range magnetic ordering from occurring. Thus to establish a probable quantum spin-liquid ground state,[85] one needs to demonstrate (1) the presence of spin interactions and have a measure of its strength such as $\theta_{\rm p}$, which establishes the presence of a spin liquid instead of a spin gas, (2) that static magnetic ordering does not occur in the accessible temperature range, (3) that a relation such as Eq. (45) is satisfied, and (4) that the lattice symmetry is not broken by the putative QSL ground state. An extensively studied example of an insulator containing Cu^{+2} spins-1/2 that satisfies these conditions is $\mathrm{ZnCu_3(OH)_6Cl_2}$ (or with deuterium replacing H), which is called herbertsmithite.[86–90]

The concept of a QSL ground state has been applied in the past to insulating spin $S = 1/2$ local-moment systems.[85] However, some itinerant spin systems such as the iron pnictides and chalcogenides and related materials are moderately correlated electron systems and sometimes have both itinerant and local-moment characteristics.[3,91–94] In such cases, we suggest that one may be able to apply the same four criteria above with respect to a possible QSL ground state. In particular, since we have demonstrated that the above four conditions are satisfied for metallic $\mathrm{SrCo_2As_2}$, we suggest that this compound has a quantum spin-liquid ground state. An alternative and very rare ground state for metallic strongly-correlated frustrated d-electron systems is a heavy-fermion ground state as observed in the cubic spinel-structure metallic compound $\mathrm{LiV_2O_4}$.[95–97] This compound shows local-moment Curie-Weiss behavior at high T and crosses over to the heavy-fermion ground state below about 10 K.

XII. SUMMARY AND CONCLUSIONS

A comprehensive study of the crystallographic, electronic, magnetic, and thermal properties of $\mathrm{SrCo_2As_2}$ single crystals is reported. The room-temperature crystal structure was confirmed to be the body-centered tetragonal $\mathrm{ThCr_2Si_2}$-type ($I4/mmm$) structure with an As–As interlayer distance intermediate between the uncollapsed- and collapsed-tetragonal values in $\mathrm{BaCo_2As_2}$ and $\mathrm{CaCo_2As_2}$, respectively. No phase transitions of any kind were detected between 1.3 and 300 K in any of our measurements, in spite of the strong negative thermal expansion of the c axis from 7.4 to 300 K and the negative volume expansion from 7.4 to ≈ 80 K. The a-axis thermal expansion is normal (positive) from 7.4 to 300 K. Furthermore, we determined from neutron diffraction measurements on a single crystal that long-range AFM order is not present at 3 K for either A-type or G-type ordering, which complements our previous determination that such ordering also does not occur at the propagation vector for stripe-type AFM ordering.[23]

The $\rho(T)$ and ARPES measurements and the LDA band structure calculations consistently demonstrate that $\mathrm{SrCo_2As_2}$ is metallic with electron Fermi surfaces centered at Γ (0,0) and on the edges of the first Brillouin zone (BZ) at $\mathbf{k} = (\pm\pi,0)$ and $\mathbf{k} = (0,\pm\pi)$. An anomalous flat band with $d_{x^2-y^2}$ character is also present in the second BZ that extends over a large fraction of the zone and results in a sharp and high peak in the electronic density of states $\mathcal{D}(E \approx E_\mathrm{F})$. This feature may be responsible for some of the anomalous properties we observe such as the negative thermal expansion and perhaps some of the T-dependent magnetic properties. The $C_\mathrm{p}(T)$ and $\frac{1}{T_1}(T)$ NMR data also exhibit metallic Fermi liquid character via the presence of a Sommerfeld electronic contribution γT and a Korringa contribution, respectively. A comparison of the measured and band structure values of γ indicates a value of the combined many-body electron-phonon and electron-electron density of states enhancements of $\approx 45\%$.

The $\chi(T)$ data show a Curie-Weiss-like T dependence above 200 K with a large negative (AFM) Weiss temperature $\theta_\mathrm{p} \sim -150$ K indicative of dominant AFM correlations in the system, consistent with our inelastic neutron scattering measurements that demonstrated the presence of strong stripe-type AFM fluctuations[23] that occur at the same wave vector as in the $A\mathrm{Fe_2As_2}$ high-T_c parent compounds.[3,10] However, our ARPES measurements and band structure calculations for $\mathrm{SrCo_2As_2}$ show no obvious Fermi surface nesting occurring at this wave vector, in contrast to the clear nesting at this wave vector in the semimetallic $A\mathrm{Fe_2As_2}$ compounds.[3] The anisotropy of $1/T_1$ determined from our NMR measurements is consistent with either stripe-type AFM spin correlations or FM spin correlations or a combination of these. At low temperatures, the $\chi(T)$ data for the two field directions show an upturn, but our NMR Knight shift measurements of the spin susceptibility show that these upturns are not intrinsic.

We modeled our $\chi(T)$ data at high T by a Curie-Weiss law and obtained values for the Curie constant and for the Weiss temperature $\theta_\mathrm{p} \sim -150$ K, which is strongly antiferromagnetic. We also modeled the data, including the broad maximum at ≈ 115 K, using a local-moment interconfigurational fluctuation model between a ground state level with spin $S = 0$ and an excited triplet state with $S = 1$, and obtained good fits to the powder-averaged $\chi(T)$ data. We further modeled the data in terms of the J_1-J_2 frustrated local-moment spin-1/2 square lattice Heisenberg model. For the latter model, a good fit to the $\chi_{ab}(T)$ data was obtained for a FM (negative) J_1, AFM J_2 and $J_2/J_1 = -1$, as suggested by the inelastic neutron scattering results,[23] with $|J_1|/k_\mathrm{B} = J_2/k_\mathrm{B} = 138$ K.

The χ for $\mathrm{SrCo_2As_2}$ has a large magnitude, roughly a factor of 3–5 larger than those of the $A\mathrm{Fe_2As_2}$ compounds in the paramagnetic state.[3] Within an itinerant magnetism picture, this suggests an even larger Stoner enhancement than in the FeAs-based compounds.[3] Moreover, the Wilson ratio for $\mathrm{SrCo_2As_2}$ is ≈ 3.5 and the Stoner criterion indicates that this compound should be an itinerant ferromagnet. A similar situation occurs in $\mathrm{BaCo_2As_2}$, where it was suggested that strong quantum fluctuations occur due to proximity to a quantum critical point that suppress long-range FM order.[24]

Thus, in $\mathrm{SrCo_2As_2}$, both FM and stripe-type AFM fluctuations/correlations appear to coexist, as also indicated by static $\chi(\mathbf{q})$ calculations that show peaks at both wave vectors.[23] This competition, the formal intermediate valence of the Co ions and the resultant quantum fluctuations may suppress the occurrence of any type of static long-range magnetic order in this compound. As discussed in Sec. XI, we suggest that metallic $\mathrm{SrCo_2As_2}$ has a gapless quantum spin-liquid (QSL) ground state. It will be very interesting to study in detail the spin excitation spectrum of this compound and compare it with those of insulating local-moment systems that are the traditional candidates for QSL ground states.

The FeAs-based and cuprate high-T_c superconductors have a common phenomenology in which long-range AFM order of the parent compounds must be largely suppressed before superconductivity appears, but where strong AFM fluctuations must still be present to act as the superconducting glue. Even though we have demonstrated that these two conditions are met in undoped $\mathrm{SrCo_2As_2}$, this compound is not superconducting above 1.8 K. Key open questions are therefore why superconductivity does not occur in $\mathrm{SrCo_2As_2}$, what the role of the FM correlations is, and whether chemical substitutions of some type or applied pressure can induce superconductivity, perhaps even at high temperatures.

ACKNOWLEDGMENTS

We thank V. K. Anand for numerous helpful discussions and A. Bostwick and E. Rotenberg for excellent support at the Advanced Light Source. V.O. thanks the Ames Laboratory–USDOE for providing the opportunity to be a visiting scientist at the Laboratory and also thanks the Russian Foundation for Basic Research (No. 12-02-31814) for support. The research at Ames Laboratory was supported by the U.S. Department of Energy, Office of Basic Energy Sciences, Division of Materials Sciences and Engineering. Ames Laboratory is operated for the U.S. Department of Energy by Iowa State University under Contract No. DE-AC02-07CH11358. Use of the National Synchrotron Light Source, Brookhaven National Laboratory, was supported by the U.S. Department of Energy, Office of Basic Energy Sciences, under contract No. DE-AC02-98CH10886. The Advanced Light Source is supported by the Director, Office of Science, Office of Basic Energy Sciences, U.S. Department of Energy under Contract No. DE-AC02-05CH11231.

[*] apandey@ameslab.gov

[†] Present address: Swiss Light Source, Paul Scherrer Institute, CH-5232 Villigen PSI, Switzerland.

[‡] johnston@ameslab.gov

[1] Y. Kamihara, T. Watanabe, M. Hirano, and H. Hosono, J. Am. Chem. Soc. **130**, 3296 (2008).

[2] C. Wang, L. Li, S. Chi, Z. Zhu, Z. Ren, Y. Li, Y. Wang, X. Lin, Y. Luo, S. Jiang, X. Xu, G. Cao, and Z. Xu, Europhys. Lett. **83**, 67006 (2008).

[3] D. C. Johnston, Adv. Phys. **59**, 803 (2010).

[4] J. Paglione and R. L. Greene, Nature Phys. **6**, 645 (2010).

[5] G. R. Stewart, Rev. Mod. Phys. **83**, 1589 (2011).

[6] J. G. Bednorz and K. A. Müller, Z. Phys. B **64**, 189 (1986).

[7] D. C. Johnston, in *Handbook of Magnetic Materials*, edited by K. H. J. Buschow, Vol. 10 (Elsevier, Amsterdam, 1997), Chap. 1, pp. 1–237.

[8] M. A. Kastner, R. J. Birgeneau, G. Shirane, and Y. Endoh, Rev. Mod. Phys. **70**, 897 (1998).

[9] P. C. Canfield and S. L. Bud'ko, Annu. Rev. Condens. Matter Phys. **1**, 27 (2010).

[10] M. D. Lumsden and A. D. Christianson, J. Phys.: Condens. Matter **22**, 203203 (2010).

[11] I. I. Mazin, D. J. Singh, M. D. Johannes, and M. H. Du, Phys. Rev. Lett. **101**, 057003 (2008).

[12] J. Dong, H. J. Zhang, G. Xu, Z. Li, G. Li, W. Z. Hu, D. Wu, G. F. Chen, X. Dai, J. L. Luo, Z. Fang, and N. L. Wang, Europhys. Lett. **83**, 27006 (2008).

[13] I. I. Mazin and J. Schmalian, Physica C **469**, 614 (2009).

[14] R. M. Fernandes, D. K. Pratt, W. Tian, J. Zarestky, A. Kreyssig, S. Nandi, M. G. Kim, A. Thaler, N. Ni, P. C. Canfield, R. J. McQueeney, J. Schmalian, and A. I. Goldman, Phys. Rev. B **81**, 140501(R) (2010).

[15] D. N. Basov and A. V. Chubukov, Nature Phys. **7**, 272 (2011).

[16] M. Rotter, M. Tegel, and D. Johrendt, Phys. Rev. Lett. **101**, 107006 (2008).

[17] A. S. Sefat, R. Jin, M. A. McGuire, B. C. Sales, D. J. Singh, and D. Mandrus, Phys. Rev. Lett. **101**, 117004 (2008).

[18] A. Leithe-Jasper, W. Schnelle, C. Geibel, and H. Rosner, Phys. Rev. Lett. **101**, 207004 (2008).

[19] S. Nandi, M. G. Kim, A. Kreyssig, R. M. Fernandes, D. K. Pratt, A. Thaler, N. Ni, S. L. Bud'ko, P. C. Canfield, J. Schmalian, R. J. McQueeney, and A. I. Goldman, Phys. Rev. Lett. **104**, 057006 (2010).

[20] S. Jiang, H. Xing, G. Xuan, C. Wang, Z. Ren, C. Feng, J. Dai, Z. Xu, and G. Cao, J. Phys.: Condens. Matter **21**, 382203 (2009).

[21] K. Matan, R. Morinaga, K. Iida, and T. J. Sato, Phys. Rev. B **79**, 054526 (2009).

[22] T. J. Sato, K. Matan, S. Ibuka, R. Morinaga, S. Chi, J. W. Lynn, A. D. Christianson, and M. D. Lumsden, Phys. Rev. B **83**, 059901(E) (2011).

[23] W. Jayasekara, Y. Lee, A. Pandey, G. S. Tucker, A. Sapkota, J. Lamsal, S. Calder, D. A. Abernathy, B. N. Harmon, A. Kreyssig, D. Vaknin, D. C. Johnston, A. I. Goldman, and R. J. McQueeney, arXiv:1306.5174.

[24] A. S. Sefat, D. J. Singh, R. Jin, M. A. McGuire, B. C. Sales, and D. Mandrus, Phys. Rev. B **79**, 024512 (2009).

[25] B. Cheng, B. F. Hu, R. H. Yuan, T. Dong, A. F. Fang, Z. G. Chen, G. Xu, Y. G. Shi, P. Zheng, J. L. Luo, and N. L. Wang, Phys. Rev. B **85**, 144426 (2012).

[26] J. J. Ying, Y. J. Yan, A. F. Wang, Z. J. Xiang, P. Cheng, G. J. Ye, and X. H. Chen, Phys. Rev. B **85**, 214414 (2012).

[27] V. K. Anand, R. S. Dhaka, D. G. Quirinale, B. G. Kim, Y. Lee, B. N. Harmon, P. W. Stephens, T. W. Heitmann, A. Kreyssig, R. J. McQueeney, A. I. Goldman, A. Kaminski, and D. C. Johnston, (unpublished).

[28] M. Pfisterer and G. Nagorsen, Z. Naturforsch. **35b**, 703 (1980); **38b**, 811 (1983).

[29] V. K. Anand, P. K. Perera, A. Pandey, R. J. Goetsch, A. Kreyssig, and D. C. Johnston, Phys. Rev. B **85**, 214523 (2012).

[30] B. Cordero, V. Gómez, A. E. Platero-Prats, M. Revés, J. Echeverría, E. Cremades, F. Barragán, and S. Alvarez, Dalton Trans. **2008**, 2832 (2008).

[31] A. Kreyssig, M. A. Green, Y. Lee, G. D. Samolyuk, P. Zajdel, J. W. Lynn, S. L. Bud'ko, M. S. Torikachvili, N. Ni, S. Nandi, J. B. Leão, S. J. Poulton, D. N. Argyriou, B. N. Harmon, R. J. McQueeney, P. C. Canfield, and A. I. Goldman, Phys. Rev. B **78**, 184517 (2008).

[32] A. I. Goldman, A. Kreyssig, K. Prokeš, D. K. Pratt, D. N. Argyriou, J. W. Lynn, S. Nandi, S. A. J. Kimber, Y. Chen, Y. B. Lee, G. Samolyuk, J. B. Leão, S. J. Poulton, S. L. Bud'ko, N. Ni, P. C. Canfield, B. N. Harmon, and R. J. McQueeney, Phys. Rev. B **79**, 024513 (2009).

[33] D. K. Pratt, Y. Zhao, S. A. J. Kimber, A. Hiess, D. N. Argyriou, C. Broholm, A. Kreyssig, S. Nandi, S. L. Bud'ko, N. Ni, P. C. Canfield, R. J. McQueeney, and A. I. Goldman, Phys. Rev. B **79**, 060510(R) (2009).

[34] R. Hu, S. L. Bud'ko, W. E. Straszheim, and P. C. Canfield, Phys. Rev. B **83**, 094520 (2011).

[35] J. Zhao, D. -X. Yao, S. Li, T. Hong, Y. Chen, S. Chang, W. Ratcliff, J. W. Lynn, H. A. Mook, G. F. Chen, J. L. Luo, N. L. Wang, E. W. Carlson, J. Hu, and P. Dai, Phys. Rev. Lett. **101**, 167203 (2008).

[36] R. A. Ewings, T. G. Perring, J. Gillett, S. D. Das, S. E. Sebastian, A. E. Taylor, T. Guidi, and A. T. Boothroyd, Phys. Rev. B **83**, 214519 (2011).

[37] N. Ni, S. L. Bud'ko, A. Kreyssig, S. Nandi, G. E. Rustan, A. I. Goldman, S. Gupta, J. D. Corbett, A. Kracher, and P. C. Canfield, Phys. Rev. B **78**, 014507 (2008).

[38] X. F. Wang, T. Wu, G. Wu, H. Chen, Y. L. Xie, J. J. Ying, Y. J. Yan, R. H. Liu, and X. H. Chen, Phys. Rev. Lett. **102**, 117005 (2009).

[39] J. Rodríguez-Carvajal, Physica B **192**, 55 (1993); see also www.ill.eu/sites/fullprof/

[40] A. C. Larson and R. B. Von Dreele, Tech. Rep. LAUR 86-748, Los Alamos National Laboratory (2004).

[41] Y. Singh, M. A. Green, Q. Huang, A. Kreyssig, R. J. McQueeney, D. C. Johnston, and A. I. Goldman, Phys. Rev. B **80**, 100403(R) (2009).

[42] P. Blaha, K. Schwarz, G. K. H. Madsen, D. Kvasnick, and J. Luitz, WIEN2K, An Augmented Plane Wave + Local Orbitals Program for Calculation Crystal Properties (K. Schwarz, TU Wien, Austria, 2001).

[43] J. P. Perdew and Y. Wang, Phys. Rev. B **45**, 13244 (1992).

[44] S. L. Bud'ko, N. Ni, and P. C. Canfield, Philos. Mag. **90**, 1219 (2010).

[45] S. L. Bud'ko, N. Ni, S. Nandi, G. M. Schmiedeshoff, and P. C. Canfield, Phys. Rev. B **79**, 054525 (2009).

[46] A. Rebello, J. J. Neumeier, Z. Gao, Y. Qi, and Y. Ma, Phys. Rev. B **86**, 104303 (2012).

[47] G. R. Stewart, Rev. Mod. Phys. **73**, 797 (2001).

[48] R. J. Goetsch, V. K. Anand, A. Pandey, and D. C. Johnston, Phys. Rev. B **85**, 054517 (2012).

[49] F. J. Blatt, *Physics of Electronic Conduction in Solids* (McGraw-Hill, New York, 1968).

[50] N. F. Mott, Proc. R. Soc. London A **153**, 699 (1936).

[51] M. Giovannini, H. Michor, E. Bauer, G. Hilscher, and P. Rogl, J. Alloys Compd. **280**, 26 (1998).

[52] D. J. Singh, Phys. Rev. B **79**, 174520 (2009).

[53] T. Kondo, R. M. Fernandes, R. Khasanov, C. Liu, A. D. Palczewski, N. Ni, M. Shi, A. Bostwick, E. Rotenberg, J. Schmalian, S. L. Bud'ko, P. C. Canfield, and A. Kaminski, Phys. Rev. B **81**, 060507(R) (2010).

[54] C. Liu, A. D. Palczewski, R. S. Dhaka, T. Kondo, R. M. Fernandes, E. D. Mun, H. Hodovanets, A. N. Thaler, J. Schmalian, S. L. Bud'ko, P. C. Canfield, and A. Kaminski, Phys. Rev. B **84**, 020509(R) (2011).

[55] R. S. Dhaka, Y. Lee, V. K. Anand, D. C. Johnston, B. N. Harmon, and A. Kaminski, Phys. Rev. B **87**, 214516 (2013).

[56] P. Mohn, *Magnetism in the Solid State: An Introduction* (Springer-Verlag, Berlin, 2003).

[57] F. Ronning, T. Klimczuk, E. D. Bauer, H. Volz, and J. D. Thompson, J. Phys.: Condens. Matter **20**, 322201 (2008).

[58] G. F. Chen, Z. Li, J. Dong, G. Li, W. Z. Hu, X. D. Zhang, X. H. Song, P. Zheng, N. L. Wang, and J. L. Luo, Phys. Rev. B **78**, 224512 (2008).

[59] C. R. Rotundu, B. Freelon, T. R. Forrest, S. D. Wilson, P. N. Valdivia, G. Pinuellas, A. Kim, J.-W. Kim, Z. Islam, E. Bourret-Courchesne, N. E. Phillips, and R. J. Birgeneau, Phys. Rev. B **82**, 144525 (2010).

[60] A. C. Jaco, J. O. Fjærestad, and B. J. Powell, Nature Phys. **5**, 422 (2009).

[61] E. S. R. Gopal, *Specific Heats at Low Temperatures* (Plenum, New York, 1966).

[62] F. Hardy, A. E. Böhmer, D. Aoki, P. Burger, T. Wolf, P. Schweiss, R. Heid, P. Adelmann, Y. X. Yao, G. Kotliar, J. Schmalian, and C. Meingast, Phys. Rev. Lett. **111**, 027002 (2013).

[63] The values of $\chi(1.8\text{ K})$ quoted for a $BaCo_2As_2$ crystal in the text of Ref. 24 and plotted in Fig. 1 of Ref. 24 were $\chi_c = 5.4 \times 10^{-3}$ and $\chi_{ab} = 3.8 \times 10^{-3}\text{cm}^3/\text{mol}$, which are 65% and 40% larger than the values that we obtained from the high-field slopes of the $M(H)$ data at 1.8 K in the inset of their Fig. 1, respectively, as quoted in our Eq. (13). These errors in the quoted values of χ_c and χ_{ab} in Ref. 24 are due to the presence of a small amount of ferromagnetic impurity in the crystal that was not accounted for, combined with the small field $H = 0.1$ T that was used to obtain the $\chi \equiv M/H$ data in their Fig. 1. Furthermore, the anisotropy obtained from their high-field measurements may be reversed compared that shown in their Fig. 1 obtained at $H = 0.1$ T and in the inset to their Fig. 1 (A. S. Sefat, private communication). In very recent measurements on single crystals [V. K. Anand, *et al.* (unpublished)], our group finds that the χ anisotropy of $BaCo_2As_2$ is reversed from that in Fig. 1 of Ref. 24 and from that in our Eqs. (13) derived from their data. For a discussion of the effects of ferromagnetic impurities on the measured M and $\chi \equiv M/H$ values of materials see Sec. 3.5.2 of Ref. 3. We thank A. S. Sefat for sending us a listing of the $M(H)$ data in the inset of Fig. 1 of Ref. 24.

[64] U. Mizutani, *Introduction to the Electron Theory of Metals* (Cambridge University Press, New York, 2003).

[65] G. Grimvall, Phys. Scr. **14**, 63 (1976).

[66] D. C. Johnston, Phys. Rev. Lett. **109**, 077201 (2012).

[67] B. C. Sales and D. K. Wohlleben, Phys. Rev. Lett. **35**, 1240 (1975).

[68] W. Franz, F. Steglich, W. Zell, D. Wohlleben, and F. Pobell, Phys. Rev. Lett. **45**, 64 (1980).

[69] J. Chaloupka and G. Khaliullin, Phys. Rev. Lett. **110**, 207205 (2013).

[70] H. Gretarsson, S. R. Saha, T. Drye, J. Paglione, J. Kim, D. Casa, T. Gog, W. Wu, S. R. Julian, and Y.-J. Kim, Phys. Rev. Lett. **110**, 047003 (2013).

[71] N. D. Mermin and H. Wagner, Phys. Rev. Lett. **17**, 1133 (1966).

[72] D. C. Johnston, R. J. McQueeney, B. Lake, A. Honecker, M. E. Zhitomirsky, R. Nath, Y. Furukawa, V. P. Antropov, and Y. Singh, Phys. Rev. B **84**, 094445 (2011).

[73] T. Yildirim, Phys. Rev. Lett. **101**, 057010 (2008).

[74] Q. Si and E. Abrahams, Phys. Rev. Lett. **101**, 076401 (2008).

[75] H. Rosner, R. R. P. Singh, W. H. Zheng, J. Oitmaa, and W. E. Pickett, Phys. Rev. B **67**, 014416 (2003).

[76] K. Kitagawa, N. Katayama, K. Ohgushi, and M. Takigawa, J. Phys. Soc. Jpn. **78**, 063706 (2009).

[77] K. Kitagawa, N. Katayama, K. Ohgushi, M. Yoshida, and M. Takigawa, J. Phys. Soc. Jpn. **77**, 114709 (2008).

[78] S.-H. Baek, N. J. Curro, T. Klimczuk, E. D. Bauer, F. Ronning, and J. D. Thompson, Phys. Rev. B **79**, 052504 (2009).

[79] F. L. Ning, K. Ahilan, T. Imai, A. S. Sefat, R. Jin, M. A. McGuire, B. C. Sales, and D. Mandrus, Phys. Rev. B **79**, 140506(R) (2009).

[80] R. R. Urbano, E. L. Green, W. G. Moulton, A. P. Reyes, P. L. Kuhns, E. M. Bittar, C. Adriano, T. M. Garitezi, L. Bufaiçal, and P. G. Pagliuso, Phys. Rev. Lett. **105**, 107001 (2010).

[81] S. Kitagawa, Y. Nakai, T. Iye, K. Ishida, Y. Kamihara, M. Hirano, and H. Hosono, Phys. Rev. B **81**, 212502 (2010).

[82] M. Hirano, Y. Yamada, T. Saito, R. Nagashima, T. Konishi, T. Toriyama, Y. Ohta, H. Fukazawa, Y. Kohori, Y. Furukawa, K. Kihou, C.-H. Lee, A. Iyo, and H. Eisaki, J. Phys. Soc. Jpn. **81**, 054704 (2012).

[83] Y. Nakai, S. Kitagawa, T. Iye, K. Ishida, Y. Kamihara, M. Hirano, and H. Hosono, Phys. Rev. B **85**, 134408 (2012).

[84] A. P. Ramirez, Annu. Rev. Mater. Sci. **24**, 453 (1994).

[85] L. Balents, Nature (London) **464**, 199 (2010).

[86] J. S. Helton, K. Matan, M. P. Shores, E. A. Nytko, B. M. Bartlett, Y. Yoshida, Y. Takano, A. Suslov, Y. Qiu, J.-H. Chung, D. G. Nocera, and Y. S. Lee, Phys. Rev. Lett. **98**, 107204 (2007).

[87] A. Olariu, P. Mendels, F. Bert, F. Duc, J. C. Trombe, M. A. de Vries, and A. Harrison, Phys. Rev. Lett. **100**, 087202 (2008).

[88] M. A. de Vries, J. R. Stewart, P. P. Deen, J. O. Piatek, G. J. Nilsen, H. M. Rønnow, and A. Harrison, Phys. Rev. Lett. **103**, 237201 (2009).

[89] T.-H. Han, J. S. Helton, S. Chu, D. G. Nocera, J. A. Rodriguez-Rivera, C. Broholm, and Y. S. Lee, Nature (London) **492**, 406 (2012).

[90] S. Yan, D. A. Huse, and S. R. White, Science **332**, 1173 (2011).

[91] P. Dai, J. Hu, and E. Dagotto, Nature Phys. **8**, 709 (2012).

[92] E. Dagotto, Rev. Mod. Phys. **85**, 849 (2013).

[93] A. Pandey, R. S. Dhaka, J. Lamsal, Y. Lee, V. K. Anand, A. Kreyssig, T. W. Heitmann, R. J. McQueeney, A. I. Goldman, B. N. Harmon, A. Kaminski, and D. C. Johnston, Phys. Rev. Lett. **108**, 087005 (2012).

[94] J. Lamsal, G. S. Tucker, T. W. Heitmann, A. Kreyssig, A. Jesche, A. Pandey, W. Tian, R. J. McQueeney, D. C. Johnston, and A. I. Goldman, Phys. Rev. B **87**, 144418 (2013).

[95] S. Kondo, D. C. Johnston, C. A. Swenson, F. Borsa, A. V. Mahajan, L. L. Miller, T. Gu, A. I. Goldman, M. B. Maple, D. A. Gajewski, E. J. Freeman, N. R. Dilley, R. P. Dickey, J. Merrin, K. Kojima, G. M. Luke, Y. J. Uemura, O. Chmaissem, and J. D. Jorgensen, Phys. Rev. Lett. **78**, 3729 (1997).

[96] For a review, see D. C. Johnston, Physica B **281-282**, 21 (2000).

[97] S.-H. Lee, Y. Qiu, C. Broholm, Y. Ueda, and J. J. Rush, Phys. Rev. Lett. **86**, 5554 (2001).